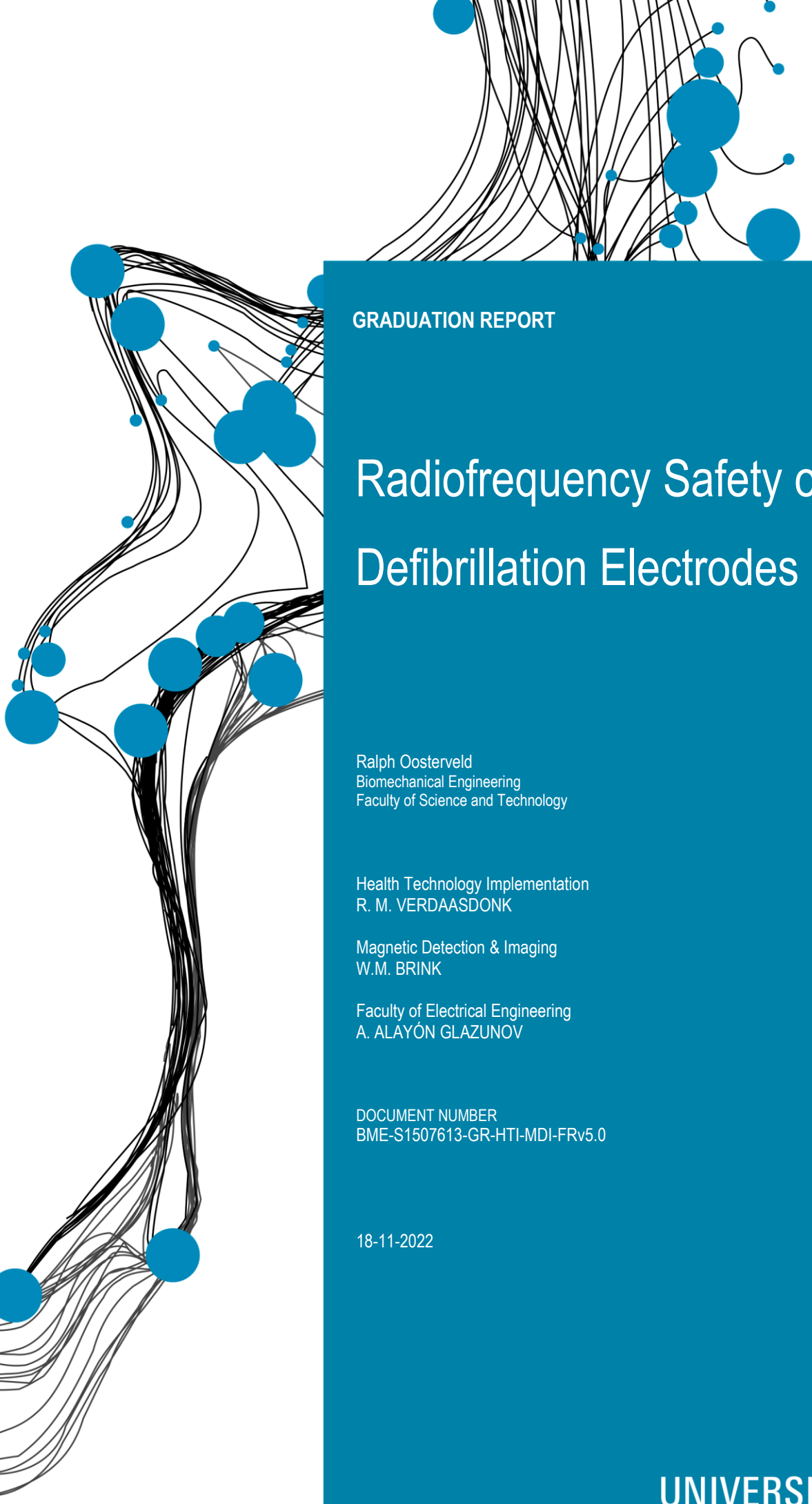

GRADUATION REPORT

Radiofrequency Safety of External Defibrillation Electrodes at 1.5T

Ralph Oosterveld
Biomechanical Engineering
Faculty of Science and Technology

Health Technology Implementation
R. M. VERDAASDONK

Magnetic Detection & Imaging
W.M. BRINK

Faculty of Electrical Engineering
A. ALAYÓN GLAZUNOV

DOCUMENT NUMBER
BME-S1507613-GR-HTI-MDI-FRv5.0

18-11-2022

UNIVERSITY OF TWENTE.

Abstract

Introduction: In health care magnetic resonance imaging (MRI) scans have become the method of choice for diagnosis of several physical conditions, but there is still a large group of patients that are excluded from MRI-diagnosis, such as patients with risk of sudden cardiac arrest (SCA). In that case immediate resuscitation is warranted. Unluckily, automatic external defibrillation (AED) devices nowadays are not compatible with MRI, because AED electrodes enhance unwanted body tissue heating. However, dividing electrodes into several parts and altering the position may diminish these thermal side effects. Therefore, this study focused on the differences in body tissue heating adjacent to the AED electrodes during MRI, comparing the positioning and use of several electrodes.

Methods: In this study the safety of external defibrillator electrodes was investigated in a two phase setup. Firstly, the effect of heating was investigated in a computer simulation, using the specific absorption rate (SAR) as outcome. Secondly, in an experiment, using a phantom as substitute for human body tissue, actual temperature changes during MRI radiation around AED electrodes were measured.

Results: In the computer simulation dividing the AED electrode in multiple transversal parts resulted in a decrease of SAR at the top and bottom of the total electrode. From one to six electrodes peak SAR values and 10-gram SAR peak values decreased from 2.18 to 1.84 W/kg (x 10^{-4}) and from 4.02 to 1.98 W/kg (x 10^{-5}) respectively. Longitudinal splitting and positioning of the electrode parts did not affect the outcomes. The peak SAR values increased with the numbers of electrode parts from 2.18 to 2.33 W/kg (x 10^{-4}) and in computation of the 10-gram SAR distribution figures grow from 4.02 to 4.39 W/kg (x 10^{-5}). In the in vitro experiment a comparable pattern was found. Transversal splitting from one to four electrodes decreased the temperature rise during MRI from 1.63 to 1.19 °C, while the longitudinal separation increased the temperature rise from 1.63 to 2.51 °C.

Conclusion: Adjacent unwanted tissue heating is prominent at the top and bottom of the AED pads, but can be reduced by the application of smaller and multiple parts of AED electrodes, that are split in the transversal plane compared to the field direction of the MRI.

Table of content

List of abbreviations

AED	automatic external defibrillation
CPR	cardiopulmonary resuscitation
cm	centimetre
°C	degree Celsius
ΔT	delta temperature
ECG	electro cardio graphic
EM	electromagnetic
F/m	farad per meter
IR	infra-red
IEC	International Electrotechnical Commission
J	joule
L	litre
MRI	magnetic resonance imaging
mK	millikelvins
RF	radiofrequency
S/m	siemens per metre
NaCl	sodium chloride
SAR	specific absorption rate
SCA	sudden cardiac arrest
T	tesla
VF	ventricular fibrillation
W/kg	watts per kilogram
w/w	weight per weight

Introduction

Clinical problem

Magnetic resonance imaging (MRI)

The development of the magnetic resonance imaging (MRI) scan represents a huge milestone for the medical world and health care. Compared to other diagnostic imaging devices it has several advantages. There is no potential harmful radiation as in X-rays, it is not invasive as tissue punctures or endoscopic investigations are, the sequence of multiple picture slides through the body can be composed to a three dimensional image for precise localization of abnormalities, and the image quality is very detailed and outstanding. For that reason, MRI often is the primary choice in diagnostics, and is continuously expanding in scope and use. MRI scans have become the method of choice for diagnosis of several physical conditions, such as cardiovascular disease, stroke, trauma and tumours. The use of MRI during surgical interventions is also continuously growing, for instance in guiding neurosurgical and cardiovascular interventions, including cardiac catheterization and electrophysiology studies[1].

MRI side effects

The MRI electromagnetic (EM) fields can pose a hazard for the patient. Even in purely biological tissues heating occurs due to the transmitted radiofrequency (RF) field. The situation becomes more complicated when a patient carries a medical implant or device sticked to the skin, in particular if this contains electrical conductive parts (Figure 1). MRI scanners are built to produce images of biological tissues, but they can't handle metallic objects, because the magnetic field induces electrical currents that are influenced by these metallic objects. The ultimate goal of the development of MRI techniques is to implement implant scanning safety concepts at the system level, so that scanners can detect an implant and respond accordingly. In this way the system can adjust the scan parameters or reject the subject[2].

Figure 1: Burn from an electrocardiographic (ECG) pad, left in place during MRI scanning.

Implant-induced human tissue heating

The application of MRI is limited in patients with implants, because of the high risk of injury from tissue heating. Magnetic RF fields applied in MRI examinations induce electrical currents in metallic implants, which cause localized tissue heating[3]. In the field of orthopedic surgery this problem occurs due to metallic materials employed in the increasing incidence of joint replacements. Research showed temperature rises up to 3.56 °C depending on type of prothesis, joint location, and MRI parameters[2 4]. However, many orthopedic implants are now made of a titanium alloy and are compatible with MRI[5]. For MRI, an implant can be considered as any foreign material or device contained in or attached to a patient's body[6], such as cardiac pacemakers, internal defibrillators, neurostimulators, implanted infusion pumps, aneurysm clips, stents, joint prostheses, catheters, electric leads, external fixation devices, and venous filters. This study focused on the influence of electrocardiographic (ECG) pads on superficial tissue heating under MRI, where research is still lacking.

Theoretical background

MRI principles

MRI uses the body's natural magnetic properties to produce detailed images of the body. The primary components of an MRI system include a magnet and radiofrequency (RF) coils[7] (Figure 2)[8]. The magnet, used to create the static magnetic field, is the largest piece of any MRI system.

To build a useful image it must produce a stable and homogeneous magnetic field throughout a certain volume of the body. RF-coils generate an oscillating/rotating magnetic field (denoted B_1) that is perpendicular to the static main magnetic field (B_0) of the magnet. In this way, the RF coils are used to generate a dynamic magnetic field that disrupts the initial static magnetic field and excites nuclear spins of protons, that can be detected to create the magnetic resonance image [9].

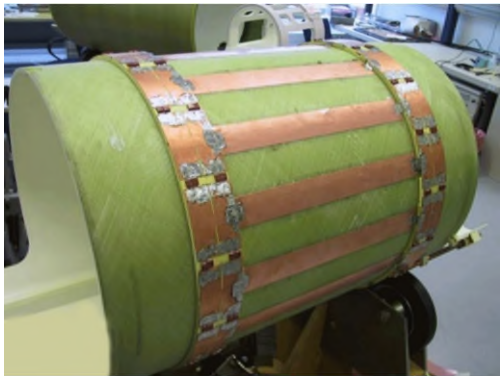

Figure 2: External view on the RF body coil.[8]

Protons are constantly spinning and so is its positive charge around it (Figure 3). This moving electrical charge generates its own magnetic field. For each proton the magnetic field is known as magnetic moments, which are normally randomly orientated (Figure 3a). However, when an external magnetic field (B_0) is applied they align either with (parallel) or against (antiparallel) the external field (Figure 3b)[10]. The preferred state of alignment is the one that requires the least energy: that is, parallel to B_0. Accordingly more protons align with B_0 than against it.

When protons are exposed to an external magnetic field they move in a particular way called precession (Figure 3b yellow arrow). The speed of precession is measured as the precession frequency (also named the Larmor frequency, ω_0)[11]. The purpose of the RF coils is to disturb the protons so that they fall out of alignment with B_0. This can only occur when the RF pulse has the same frequency as the precession frequency of the protons, a phenomenon called resonance. Therefore, RF pulses are set at the Larmor frequency. The composition of MR images is based on these changes in proton direction and spin, caused by the EM field, but will not further be described, because this is beyond the scope of and irrelevant for this study.

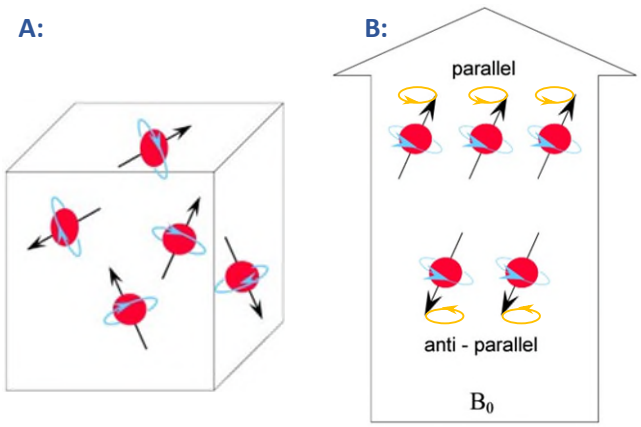

Figure 3: Protons (red) possess a positive charge (blue arrow) and are constantly spinning around their own axes. A) Normal magnetic moments of the protons are randomly oriented. B) Placed in an external magnetic field (B_0) the protons align parallel or anti-parallel to the field direction. The overall effect on a group of protons means that the group of spins classically move in a particular way called precession (yellow arrow).

RF coils

MRI relies on time-varying magnetic fields that differ in frequency and amplitude. The so called sinusoidal RF field B_1 is required to excite the spins to be imaged[12]. The field is generated by a RF coil inside the scanner's bore . Its main focus is to get a homogeneous B_1 field.

The cylindrical birdcage coil is the most commonly used RF-transmit device in MRI[13] (Figure 4a). It consists of two circular conductive loops referred to as end rings, connected by an even number of conductive straight elements called rungs. The number of rungs depends on the size of the coil. In transmit operation sinusoidal currents are applied to each rung that are sequentially phase shifted around the coil's periphery.

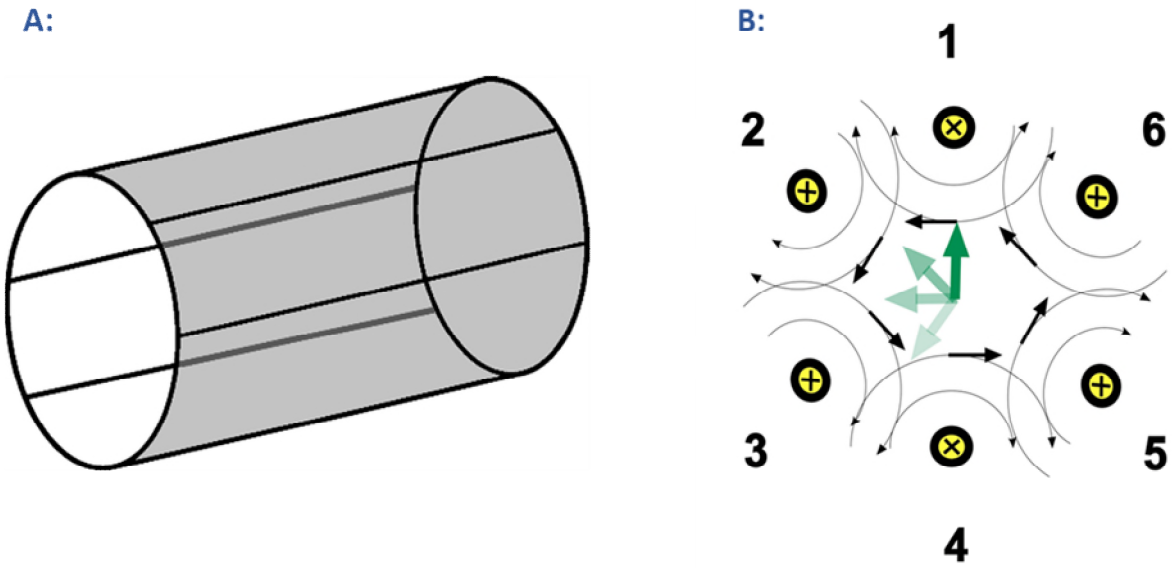

Figure 4: a) Simulated model of a simplified six rung MRI birdcage coil. b) Crosscection of the birdcage coil showing the generation of the rotating B_1 field (green arrows in centre). Sinusoidal current that is applied sequentially to the rungs generates a local field. The phase shifts between the successive rungs produces a resonantly rotating B_1 field.[8]

Figure 4b shows an example of a 6-rung birdcage coil in cross section. Each rung is powered by a sinusoidal current that will create a local EM field around each rung. The phase shift between the currents in neighboring elements is 360°/N, where N is the number of rungs (six in this example). As each rung peaks in turn, the central magnetic B_1 field is seen to rotate[14].

Eddy currents

All time-varying EM fields around the separate rungs are accompanied by perpendicular electric fields, that can be visualized as "curling around" the magnetic field in concentric loops; the so called eddy currents[15] (Figure 5). Both magnetic and electric fields oscillate at the same frequency, so the direction is rapidly switching from clockwise to counter clockwise in each cycle. So, changing magnetic fields generate eddy currents in accordance with Faraday's law of induction. When these currents encounter electrical resistance, for instance in biological tissue, thermal energy is produced[16].

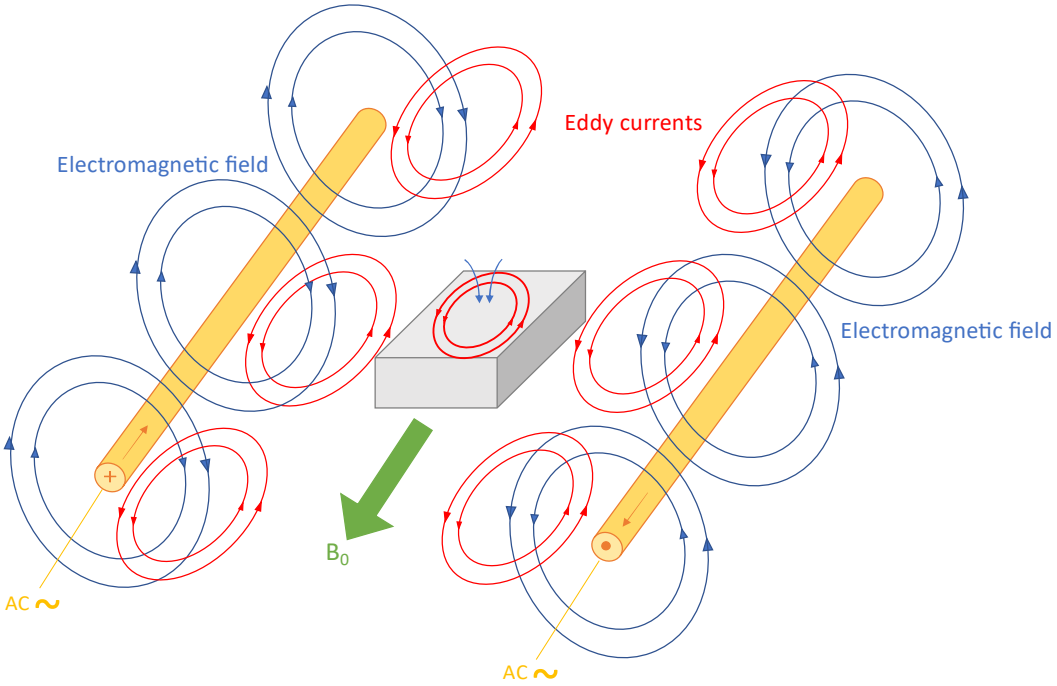

Figure 5: Representing only two RF coils (left and right in yellow) in the birdcage coil. Eddy currents (red) are generated around the magnetic field produced by the MRI coil in a nearby birdcage rung, whenever a changing magnetic field is present.

In Figure 5 each opposite coil differs 180° in phase. If the left one is in a positive current, the right one has an negative current, which results in a clockwise EM field around the left and a counter-clockwise EM field a round the right coil. In fact, within the two coils the both EM field directions are the same, running top-down. The eddy currents, generated through this EM field, has a field direction perpendicular to B_0 and parallel to the B_1 field. Close to the coils, the magnetic field is stronger and therefore, the created currents will also be greater close to the MRI bore, compared to its centre point.

Tissue heating

Under continuous RF exposure and without heat dissipation, the local tissue temperature would rise linearly in time with the absorbed RF power per exposed mass, following the so called specific absorption rate (SAR) formula

$$\mathrm{SAR} = \frac{\sigma A^2 \omega^2 \beta_1^2 D}{2\rho} \qquad (1)$$

where σ is the electrical conductivity, A denotes the body cross-sectional area and the mass density is given by ρ, which are tissue parameters. The other parameters describe the transmit coil, which include magnetic field frequency ω, direction of B_1 and the duty cycle D. SAR is a local quantity and must be computed for all isolated spots on the body and is expressed in W/kg. So, the SAR figure depends on all local parameters and is influenced, i.e. by body tissue structure and possible presence and shape of the implants. SAR is usually averaged over the whole body (global SAR) or a small sample of volume, usually 1-gram or 10-gram of tissue (local SAR)[17]. Averaging the deposited power by the coil over the whole sample exposed by the RF coil leads to global SAR. The global SAR reflects the total power deposited in the tissue. This 10-gram SAR is a better estimate for tissue heating than 1-gram SAR over a wide range of frequencies and for near and far field exposure[18].

The electric fields of independent channels can constructively interfere at points in the body and create local hot spots, whose effect is quantified by local SAR. The peak local SAR inside the body needs to be kept under specified safety limits, hence a large number of constraints are forced upon the RF pulse[17]. There are regulatory guidelines that define acceptable limits of SAR in the human body[19]. In most countries, MRI systems are limited to a global maximum SAR of 4W per kg, which in general does not cause safety issues for patients or influence clinical practice. However, for specific patients with (active or passive) implants or needing special electrocardiographic (ECG) heartrate monitoring surveillance in the case of cardiovascular diseases, extra attention is required, because these implants or devices may locally increase SAR. Compliance with these SAR limits can impose restrictions on the duty-cycle and/or the power of the transmitted RF pulses, potentially leading to longer scan times or altered and inferior contrast of images.

Peripheral AED electrode heating

Highly conductive materials such as metals, induce a scattered field, as in the case of an AED electrode, which locally increases the electric field strength and creates higher SAR values at the bottom and the top (yellow in Figure 6c).In fact, the regular electric field (Figure 6a) is disrupted by the highly conductive electrode and "pulls" the field towards it (Figure 6b and Figure 6c).

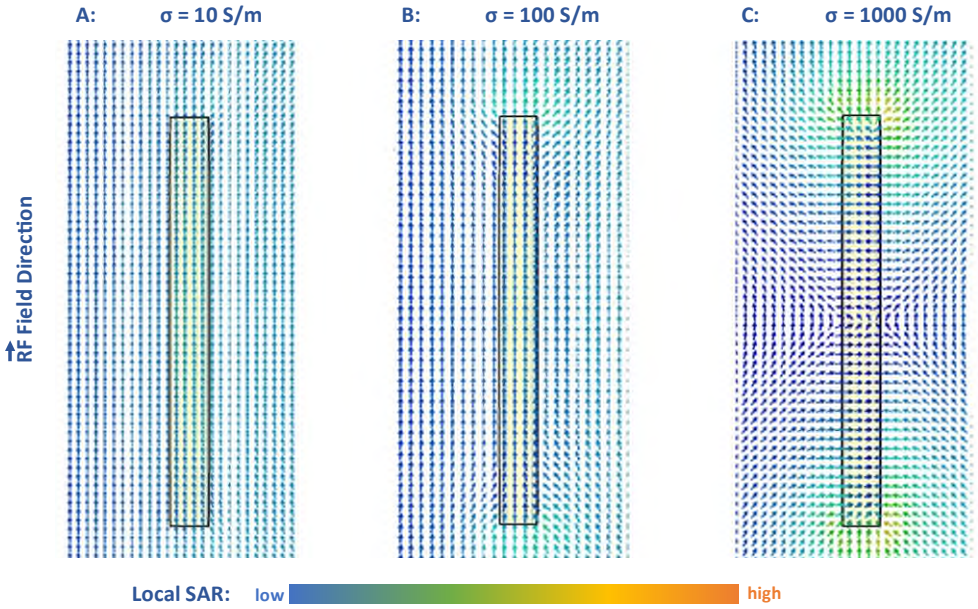

Figure 6: Simulation of electrodes or implants with different conductivity inside the magnetic field. From left to right (a to c), the increasing conductivity (σ) of the implant is shown above in each figure. For low conductivity objects eddy currents are still able to penetrate the material without consequences. Metals with high conductivity create a scattered field, that will result in higher SAR values at the tips.

RF-induced eddy currents only flow through a tiny fraction of the total electrode mass at its surface and does not cause direct heating of this foreign material[20]. However, in the soft tissues immediately adjacent to the electrode, where electric fields and currents are concentrated, very high levels of heating can occur. In phantom experiments, the temperature at the tip of a long wire increased by 75 °C, but in clinical situations temperature rises are limited within the range of one to three degrees °C. Nevertheless, this heating may lead to tissue damage, for instance increasing the risk of prothesis loosening.[2]

Higher risks of heating occurs in materials with large surface areas and high conductivity, because large numbers of closed eddy current loops can develop (Figure 7a). These currents can be minimized by splitting electrodes into parts and adding isolating slots in its conductor surface (Figure 7b). Then, electrons cannot cross the insulating gap between these laminations and so are unable to circulate on wide arcs. This results in a higher total resistance of the material, so less currents are flowing through the object.

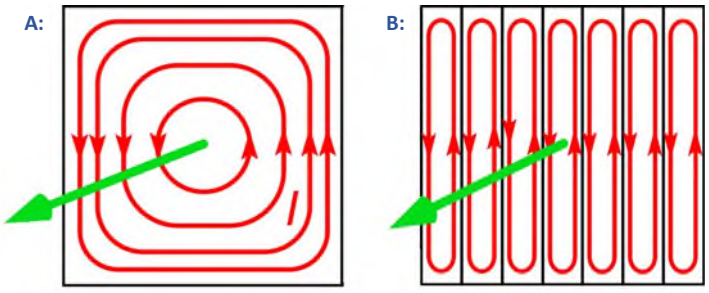

Figure 7: a) Optimal field of closed eddy currents loops (red) within solid material. b) A separated and diminished field of eddy currents loops within each material part. Lamination creates insulation that lowers the conductivity of the whole material, so eddy currents are minimized (red). The green arrow represents the EM field direction.

State of the art clinical solutions

Patient's safety

During an MRI examination patient safety is of great importance. Given the properties of the MRI environment, specific protocols are in place in order to protect the patient[21]. Monitoring consists of several vital signs, such as blood pressure, respiration, body temperature and cardiovascular function. These vital signs must be monitored if the patient is either undergoing an interventional MRI, injected with a contrast agent, sedated or under anesthesia, or when the patient is in critical care. Previously, under these safety regulations and precautions, MRI diagnosis in patients with pacemaker implants was not possible, but new technological innovation has driven the progress of implants. Recent cardiac pacemaker models compatible with MRI, allow patients to access scanning under well-defined conditions[22].

MRI and cardiovascular conditions

There is still a large group of patients that are excluded from MRI-diagnosis or guided interventions. Patients who are hemodynamically unstable, suffer from subacute or acute ischemia, or experience severe heart failure, have contraindications that in many places lead to exclusion from MRI diagnosis[23]. The main reason for the exclusions is the current inability to quickly detect and promptly intervene in the case of a cardiac event in the MRI bore. A sudden cardiac arrest (SCA) occurring in the bore involves removing the patient from the bore, removing the head or body coils if present and transferring the patient from the MRI table to a transport stretcher or disconnecting the MRI table to use for transport. When the patient has been removed to a designated safe location, then it is possible to begin attaching defibrillation electrodes to deliver the defibrillation pulses. This sequence delays the start of defibrillation by several minutes and significantly increases the risk of mortality, because the survival rate is reduced by 5.5% every minute[24].

Cardiac arrest under MRI

Being able to detect an early cardiac malfunction under MRI by means of an electrocardiograph (ECG) is warranted and requires development of equipment that does not interfere with the technical and diagnostic properties of the MRI or expose patients to the risk of superficial skin burning around electrodes. For rapid detection of a cardiac event in high-risk patients, nowadays MRI-compatible ECG systems and systems that can detect hemodynamic and oxygen emergencies are available. Previous studies have shown that a 12-lead ECG is possible during MRI[25]. This 12-lead ECG (Figure 8a) is the standard care for cardiac physiological monitoring and may be required during intervention on cardiac patients. In order to allow for cardiac imaging, MRI scanner manufacturers currently provide 3-4 lead MRI-conditional ECG systems (Figure 8b)[26]. These MRI conditional ECG electrodes use high-impedance lead wirers and are placed at small distances, what will reduce the RF induction into the body around the ECG leads. So, conventional 12-lead ECG's is the standard in quality and in the near future even possible in MRI; the current intra-MRI 4-lead ECG's are mainly applicable for acquisition synchronization, and not for physiological monitoring[27]. Having solved the problem of adequate cardio monitoring under MRI, the next challenge is the development of in MRI applicable defibrillation pads and equipment.

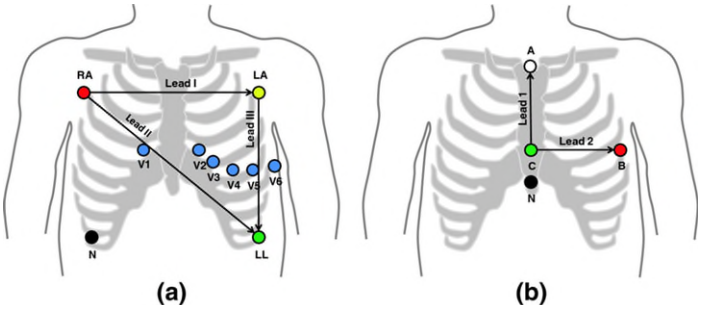

Figure 8: Number of electrodes with its positioning comparing 12 and 4 lead ECG systems. a) The standard 12-lead configuration is used for monitoring cardiac patients. b) A typical MRI conditional ECG system application uses a reduced orthogonal configuration of 3 to 4 leads.

Automated external defibrillation (AED) and MRI

Defibrillation is the most effective treatment for severe ventricular fibrillation (VF) that causes circular blood flow insufficiency and may lead to a SCA; the longer a patient has to wait for a defibrillation shock, the lower the chances of survival. Modern defibrillators create biphasic discharge curves that compensate for chest wall impedance to lower the total energy used while maintaining efficacy. Impedance-based defibrillation refers to the adjustment of shock waveform features or shock energy based on patient resistance. Because defibrillation thresholds vary substantially from patient to patient, this feature results in a more efficient use of energy. Subsequently, cardiopulmonary resuscitation (CPR) is necessary to maintain blood flow to and through vital organs to prevent ischemia and irreversible damage[28]. However, defibrillation is always required to regain heart function, because CPR alone cannot restore a normal heart rhythm. Therefore, due to patient safety concerns, individuals at risk for life-threatening heart failures nowadays cannot undergo MRI-guided interventions or diagnosis.

Influence of AED-pad size

Larger electrode pad sizes have been shown to reduce transthoracic impedance and improve defibrillation success rates. Electrode pad size is an important determinant of transthoracic current flow during the external countershock. Dalzell et al. used self-adhesive, dual function electrocardiogram/defibrillator pads to assess the effect of electrode pad size on defibrillation success with low energy (200 J) shocks[29]. Three pad size diameters from 8 cm up to 12 cm were compared in success rate relative to its transthoracic impedance measured before defibrillation. The first shock of 200 J was successful in 31% using small pads, 63% for intermediate pads and 82% with large pads. A second 200 J shock increased the success rate to 46%, 79% and 97% respectively. Transthoracic impedance decreased with increasing pad size and improved defibrillation success rates with low energy shocks.

Risk of AED-pads in MRI

Heating around the area of the AED pad can occur due to RF radiation and also during the possible electrical defibrillation pulse. An MRI-conditional cardiac defibrillator should allow scanning with defibrillation pads attached to a patient, enabling application of defibrillation within seconds after a cardiac event inside the MRI. Pilot animal studies with porcine subjects have demonstrated the feasibility of low (200 J) and high-energy (360 J) in-bore defibrillation discharges, using modified high voltage twisted pair cables equipped with RF baluns[23]. Limited insights have yet been established in terms of MRI safety of these devices, in particular, RF heating during high SAR sequences. Even in short exposure durations of 6 to 11 minutes, skin alterations such as redness as well as deeper lesions were observed, indicating potential deleterious effects[30]. As a requirement from the Food and Drug Administration, it is demanded that the defibrillation surface pads do not increase in temperature over 1.5°C during imaging with high (4 W/kg) SAR MRI sequences of 15 minutes[31]. According to the International Electrotechnical Commission (IEC), the upper SAR limit in normal operating mode is 2 W/kg averaged over 6 minutes[32].

Recent development

Rapid detection of a VF or a cardiac arrest is possible during an MRI scan, but the application of external defibrillation is currently clinically still impossible, because commercially available external defibrillators cannot be used in the MRI environment. This absence of an MRI-compatible defibrillator, that can provide immediate defibrillation in the magnet bore hinders the application of MRI investigation in high-risk patients, as well as to perform cardiovascular procedures under MRI guidance that may require external defibrillation or cardioversion in the case of emergency. However, the feasibility of in-bore defibrillation has been demonstrated in a pilot study for intermediate-energy (200 J) levels, what is a frequently used energy level for the first discharge. These experiments were conducted using a commercial defibrillator with a custom high-voltage, twisted pair cables and a

custom radiofrequency (RF) emissions filtering setup[23]. Shusterman et al. designed a demonstrator of an external defibrillation system, that is safe to use in the bore of a clinical MRI scanner[33]. In addition, external defibrillation is possible during active MRI scans. However, caution should be exercised when performing defibrillation with standardized electrode properties, which in certain configurations can lead to tissue heating under the pads.

Research Questions

One of the most acute technical missions is to develop an external defibrillation device suitable for the use during an MRI procedure so the risk for cardiac patients during an MRI scan will be reduced. Therefore, RF heating around electrodes must be substantially diminished, probably by dividing the electrodes into parts, that may result in reduced RF eddy currents. It is possible to split the AED pads into multiple parts, with regards to the totally required superficial magnitude, necessary for the effective peak current during defibrillation. However, if the application of numerous electrodes definitely leads to reduced RF heating is unknown. Investigating that issue is the aim of this study.

Reducing the RF heating around the AED electrodes attached to the human body may theoretically and empirically be accomplished by dividing the large electrode in smaller sectors and changing the orientation of those sectors. Therefore, the general research question for this study is defined as follows:

"Is there any difference in body tissue heating adjacent to the AED electrodes during magnetic resonance imaging comparing the use of a single to several electrodes?"

Sub questions are:

1. *Is the magnitude of the tissue heating adjacent to an AED electrode affected by its positioning on the phantom and its position within the MRI coil?*
2. *Is the magnitude of the tissue heating adjacent to an AED electrode affected by the metric area or the amount of electrodes used?*
3. *Has the transversal or the longitudinal splitting of the electrodes an effect on tissue heating?*

These research question were initially investigated using COMSOL computer simulation. Findings from the simulation were used for further development of the final in vitro study using a human-like phantom.

Materials and Methods

General study design

In this study the RF safety of external defibrillator electrodes was investigated in a two phase setup. Firstly, the effect of RF heating was investigated in a computer simulation. Secondly, in an experiment, using a phantom as substitute for human body tissue, actual temperature changes around AED electrodes were measured during MRI radiation.

Computer simulation

Study design

The setup and environment of a clinical MRI investigation was rebuild in a COMSOL computer model, using a simulated virtual phantom, representing the human body with thorax and internal organs as heart and lungs, with electrodes attached. The COMSOL model offers the possibility to simulate the whole MRI procedure and compute estimates of the physical and physiological effects or unwanted side-effects. In this study a simulation focussing only on consequences of the RF radiation was established, particularly on adjacent heating of AED electrodes. The temperature was estimated calculating the specific absorption rate (SAR). Firstly, using one electrode, the tissue peak temperature over the virtual phantom was identified by moving the electrode location into 25 different pre-defined positions, i.e. by combining 5 transversal and 5 longitudinal positions in a regular grid. Subsequently, seven simulations were run testing the use of several electrodes (from one up to six) and their influence on tissue heating. Additionally, the impact of longitudinal or transversal positioning of the AED pads within the RF radiation field was investigated. So, in fact simulations with one, two, four and six electrodes transversal and longitudinal, with a separation of 3 mm were run.

COMSOL simulation

COMSOL Multyphysics®[I] software platform creates physics-based models and simulation applications. Its model builder application enables to combine multiple physics in any order for simulations of real-world phenomena and was enhanced with the RF module [I] for this study. The RF Module of COMSOL solves problems in the general field of EM waves. It allows to quickly and accurately predict EM field distributions, transmission, reflection, and power dissipation in a proposed design.

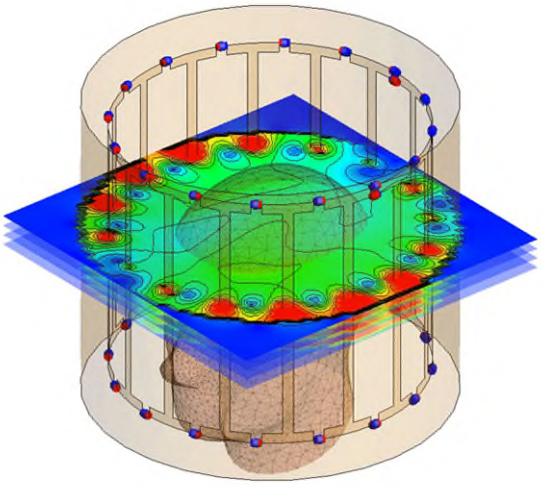

Figure 9: Electromagnetic wave cross-sections simulations within an MRI head coil. [2]

MR imaging

COMSOL Multiphysics® software is able to design models in which the magnetic field can be manipulated and measured. MRI systems must provide images capable of producing accurate diagnosis. To achieve this level of image quality, MRI requires a homogeneous high magnetic field within the MRI machine and its components, such as birdcage coils[34] (Figure 9)[II]. So, it can be used to design an MRI coil and optimize the magnetic field around a virtual phantom to create the desired distribution.

[I] COMSOL BV, Röntgenlaan 37, 2719 DX Zoetermeer, Netherlands, info-nl@comsol.com. Software version 5.6
[II] Altair (Feko) Engineering Inc. Attn: General Counsel, 1820 E. Big Beaver Road, Troy, MI 48083

Phantom simulation model

Virtually a phantom with dimensions of 30 x 40 x 20 cm^3 was placed inside the birdcage coil model to mimic the human body ,which skin has a conductivity (σ) of 0.45 S/m[35 36]. Additionally, also an estimate of the permittivity (ε_r) of the human body was made and in this case set on 45 F/m, what is in range of typical naturel values[37]. Although the average density of the human body is 985 kg/m³, in this computer simulation a density (ρ) of 1000 kg/m³ was chosen to enable comparison between this COMSOL computer simulation and the later in vitro MRI experiment, because of the water based phantom[38].

AED electrode simulation model

The standard clinically used available AED pads have dimensions from 8 to 12 cm^2 with rounded corners[29]. For this simulation a simplification of the AED pad geometry into straight angles has been made to enable accurate computations and easier comparisons across the variety of simulations (Figure 10). In the COMSOL model the AED pad was simulated as a metal sheet of 8 by 12 cm^2.

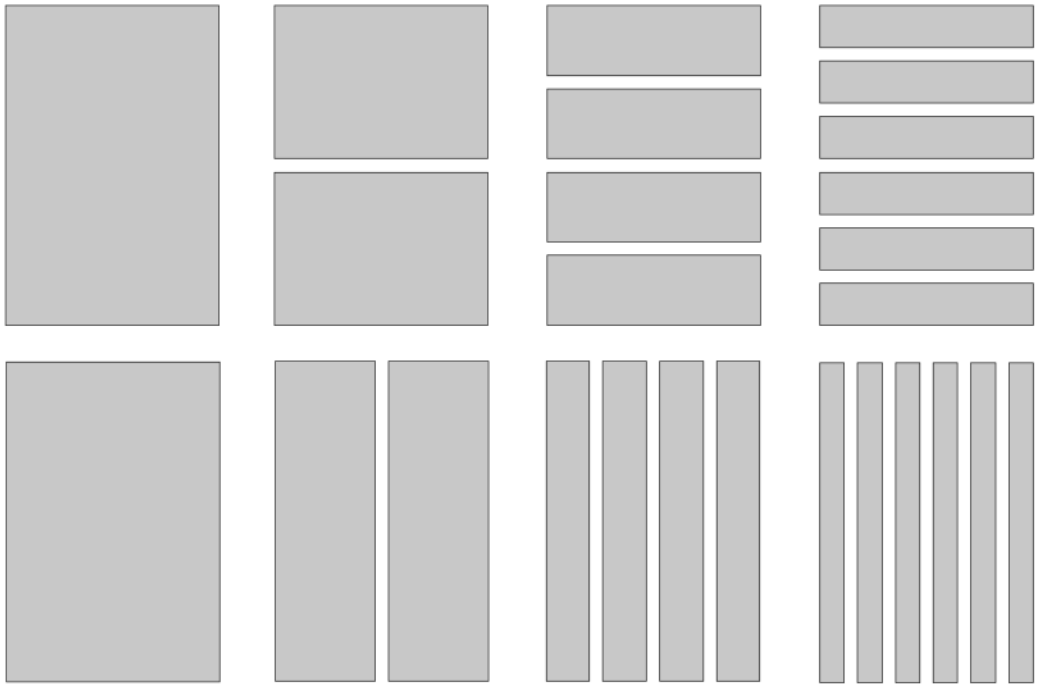

Figure 10: Display of the simulated sequence of splitting the AED electrodes. On top, the division into transversal parts. Below, division into longitudinal parts.

To accurately represent the electrode's adhesive, a film layer of 1 mm over the complete upper surface (30 by 40 cm) of the virtual phantom was simulated with a permittivity ε_r = 2.5 F/m and a conductivity σ = 0.05 S/m[39]. Because of this rather thin adhesive layer the mesh resolution around the virtual phantom interface was increased to get a minimum element size of 0.5 mm.

MRI coil simulation model

In this simulation, the technical parameters similar to the MRI device used in the in vitro experiment were applied. The radius and the hight were defined on 35 cm and 50 cm respectively. The birdcage model (Figure 11) consists of eight rungs, which are 6 degrees in width and each lumped element in the centre of the rungs measured 1 cm. The lumped ports are designed to get a normalized field with a power output of 1V and impedance of 50 Ω. For a 1.5 T machine, the resonant frequency is 64 MHz. To run the COMSOL computer model, some parameters are required and must be set according to known data from clinical practice or otherwise estimates had to be made.

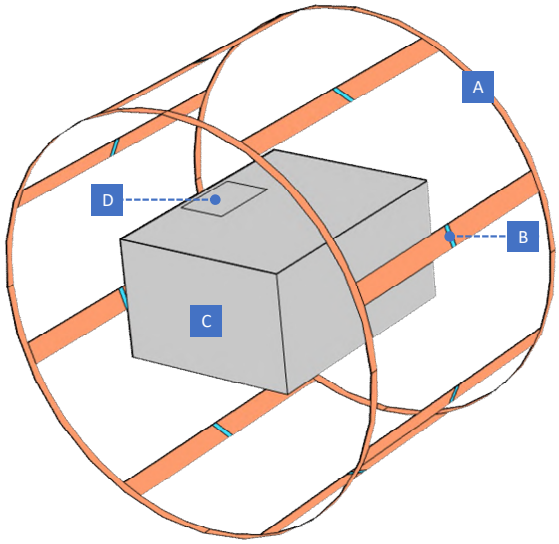

Figure 11: COMSOL MRI birdcage model. The birdcage coil (a) with lumped elements (b) on the rungs. Insite the bore centre is the phantom (c) with placement of the AED electrode (d).

An efficient RF magnetic field is obtained with a coil that produces a RF field with circular polarization. Starting with two sets of linearly polarized coils (four in total) perpendicular to each other and driving them with sinusoidal currents phase-shifted by 90°, a circular polarized B_1 field can be created with no wasted power. To go from four to an eight coil birdcage, another set of these 4 coils are positioned in an angle of 45° and driving an added shifted phase of ¼pi to the first set of coils, so a more homogeneous field is created. Figure 11 shows the geometry of the model, which consists of a birdcage coil with 8 lumped elements placed around a virtual phantom.

SAR computation

In this simulation the heating of body tissue was estimated by the computation of SAR which is very complex and requires advanced mathematical modelling. However, the COMSOL software performs fast and accurate numerical computations if all the required input parameters are correctly defined. The local SAR was computed for every 0.5 mm^3 (mesh size) using the theoretical SAR formula as describe previously in the introduction, in which COMSOL maintains the following quotation

$$\mathrm{SAR} = \frac{\sigma |E|^2}{2\rho} \qquad (2)$$

where σ is the conductivity, ρ the density, and |E| the effective magnitude of the electric field. The latter depends on, and incorporates various parameters e.g. the body cross-sectional area *A*, the RF frequency *ω*, the flip angle of the MR sequence and the duty cycle *D*.

All the local SAR values within the total volume of the virtual phantom were exported from COMSOL to MATLAB[III] and were used to estimate the 10-gram SAR values. The combined results were produced to provide a general picture by means of cross-sectional visualisation as explained in Appendix A. With the assumed density ρ = 1000 kg/m^3 and the dimensions of the virtual phantom, the mass was computed per voxel volume, the smallest detectable element of a 3D object. This 1-gram SAR data matrix was converted into 10-gram SAR data by means of a SAR averaging function presented in Appendix B. The obtained SAR values are distributed within the whole volume of the virtual phantom.

[III] MathWorks - Natick, Massachusetts, United States

Then, a superficial cross section was made. Because temperature images were used in the in vitro experiment, an identical cross section in MATLAB was employed in order to compare the results.

MRI experiment

Research design

The in vitro experiment was performed using a Siemens MRI Magnetom Aera 1.5 T[IV]. The knowledge from the previous computer simulation was used as reference for the design of the MRI experiment and same parameters were used to ensure comparability between CONSOL simulation and in vitro experiment. For instance the comparison between the various used numbers of AED electrodes was limited to four in total, because in the simulation no substantial difference in tissue heating was found comparing the application of four to six electrodes (see results section). The heat distribution on a phantom, mimicking the human body, was measured by a FLIR Infra-Red (IR) camera with thermal resolution of 19200 pixels and sensitivity 100 mK[V] before and directly after MRI. Subsequently six measurement sessions were performed:

- MRI experiment without electrodes
- MRI experiment with one standard electrode
- MRI experiment with 2 transversal positioned electrodes
- MRI experiment with 4 transversal positioned electrodes
- MRI experiment with 2 longitudinal positioned electrodes
- MRI experiment with 4 longitudinal positioned electrodes

Temperature changes between sessions were compared and peak values of temperature were localized using MATLAB (for calculations and specific algorithms see Appendix C).

Materials

MRI specifications

During the measurements in a Siemens Magnetom Aera 1.5 T, a phantom was continuously scanned for 20 minutes, using MRI sequences at the maximal allowed global SAR (4 W/kg).

Phantom properties

The phantom (21 x 33 x 8 cm^3) used in this in vitro experiment had the same properties as the model used in the COMSOL simulations. This phantom was constructed from agar, that provides a useful way of testing bio-impedance imaging systems. These type of phantoms can be physically molded and their electrical properties can be altered to mimic a variety of tissue types and anatomical configurations. The conductive properties of these phantoms can be controlled by the concentration of NaCl used in their preparation. A 5 L rectangular phantom was made consisting of agarose gel (2% w/w) with NaCl for electrical human-like conductivity adjustment. The phantom was constructed of 3.5 L water and 1.5 L saline with NaCl 0.9% solution to get a conductivity of 0.45 S/m matching that of the average conductivity of the human body, as was done in the previous COMSOL simulation. During every measurement the phantom was placed at the same location in the center of the MRI bore.

[IV] Siemens Healthineers Nederland B.V., Prinses Beatrixlaan 800, P.O. Box 16068, 2500 BB The Hague.
[V] Teledyne FLIR Systems, FLIR One Pro-series for IOS - Wilsonville, Oregon, Verenigde Staten

AED electrodes

For this experiment standard AED electrodes of 8.5 x 12 cm² (approx. 85 cm²) with rounded corners were used (Figure 12). The cable of the AED pad was removed, so only the impact of the contact area with the phantom tissue was investigated. During the experiment, the electrodes were divided into parts. The first electrode was cut transversally to create 2 parts of 8.5 x 6 cm². These two were then divided into 4 transversal parts of approximately 8.5 x 3 cm². Another electrode was split into longitudinal parts. First, into two longitudinal parts of about 4 x 12 cm², that were further divided into 4 parts of roughly 2 x 12 cm². All the electrodes were placed at the same location (position d) as shown in Figure 11. This position is the left center side, so the electrode is located 1 cm from the phantom edge. Split AED electrodes were placed 3 millimeters apart as was done in the previous simulations.

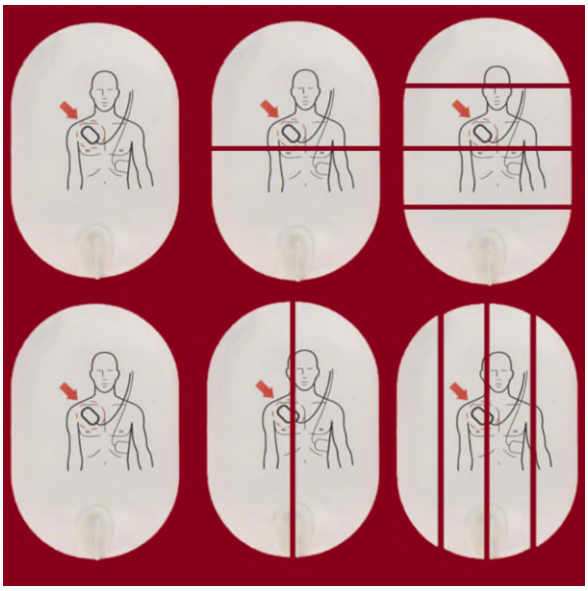

Figure 12: Method of splitting AED electrodes. On top: dividing the electrode in transversal direction of 2 and 4 parts. On the bottom, dividing the electrode in longitudinal direction, first 2 then 4 parts.

IR temperature sensor calibration

For this setup the FLIR IR camera was used to measure the temperature changes in the phantom. This thermal camera has a temperature resolution of 0.1 °C. It measures temperature changes with a high accuracy and precision of 0.3 °C, which is not a random, but with a systematic error. This means that a divergent temperature reading of e.g. +0.2 °C will be stable during the whole measurement procedure. For reliable usage of these cameras in clinical applications and this experiment a fast quality pre-measurement calibration is required: previous studies have shown that absolute temperature measurements are closer to the actual value when the sensor has already been recording for several minutes[40]. Therefore, measurements were not started until temperature readings stabilized.

To validate the IR temperature measurements and adjust for the systematic precision error, additional PT100 sensors[VI] were applied. Two PT100 sensors were used to provide the actual temperature at two reference points and compared with the IR camera image recording in order to enable proper calibration.

[VI] CENTER Technology Corp. 4F, No.415, Jung-Jeng Road, Shu-Lin Dist., New Taipei City 238, Taiwan.

IR temperature measurement

For reliable temperature recordings before and after every MRI session a specific setup was developed to standardize measurements as shown in Figure 13. For every measurement the phantom was placed in an identical way and spot on a prepared frame to ensure comparable repeated measurements. In this way, every time the IR camera was positioned exactly above the center of the phantom at 80 cm to ensure full coverage of the phantoms surface. For calibration purposes the two PT100 temperature sensors were placed beside the phantom. Firstly, before and after the 20 minutes MRI scan, the phantom temperatures were captured without any AED pad. Then a generic AED electrode[VII] of 8.5 × 12 cm² was positioned on top of the phantom, and subsequently replaced by modified electrodes; starting with the transversal and longitudinal 2 parts electrodes followed by the four part electrodes. So, the measurement sequence was:

- T0 – MRI scan without electrode
- T1 – MRI scan with standard electrode
- H2 – MRI scan with 2 parts transversal electrode
- V2 – MRI scan with 2 parts longitudinal electrode
- V4 – MRI scan with 4 parts longitudinal electrode
- H4 – MRI scan with 4 parts transversal electrode

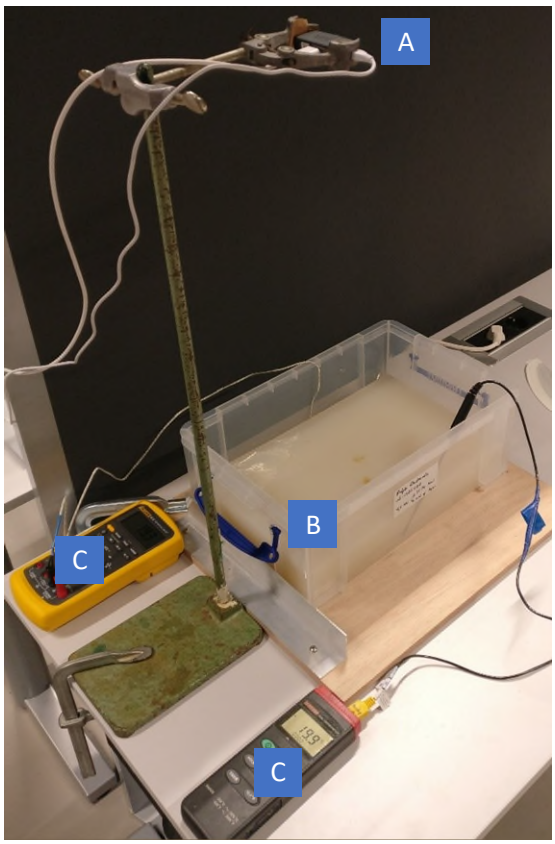

Figure 13: Experimental setup to measure temperature with IR camera(a), the agar phantom (b) and two temperature sensors (c) for verification of the measurement results.

When the phantom was inside the MRI for a scan, a second reference phantom (with identical properties) was placed underneath the IR temperature camera to maintain a stable IR picture. This duplicated phantom ensured that the possible temperature differences in the IR image during the MRI scan time did not deviate from the initial pre-scan measurement of the phantom. At the beginning of the experiment, both phantoms were stored at an ambient temperature of 21 °C. The average time between two MRI scans was 5 minutes. During this time the phantom was removed from the MRI bore and placed under the IR sensor. Then the AED electrodes were removed so that the phantom temperature could be measured. Also, the PT100 sensor values were noted for verification. After this had been recorded, the next AED electrode was positioned on the phantom, that was placed back in the central location in the MRI for the next session and measurement.

[VII] Heartstart FR2, Philips Healthcare, Best, the Netherlands

Results

COMSOL simulations

The results of the COMSOL simulation are expressed in figures to enable better visual interpretation of the tissue heating under MRI application. Besides that, absolute outcomes of SAR computation are also presented in tables.

Phantom heating pattern

In order to evaluate the virtual phantom heating pattern differences due to AED pad designs, positioning or size of the electrodes, it was decided to use the “worst case” location, i.e. the location on the virtual phantom surface with highest tissue temperature increase. In Figure 14 the virtual phantom surface is shown based on the maximum 1-gram SAR value on that specific location. The magnitude of the SAR value depends on the direction of eddy currents and distance to the coil rim, because SAR tends to be more concentrated around the periphery, as previously explained in the “theoretical background” in the “introduction". In the perspective from the bottom of the image in Figure 14, the simulated EM field turns counter clockwise. So at the left side, coming from above EM energy is firstly absorbed by the AED electrode and then by the virtual phantom substance. At the right side the opposite occurs and some energy is absorbed by the virtual phantom before the AED electrode is reached. Therefore, the effect on development of eddy currents causing higher SAR values is more predominant at the left than at the right side of the image.

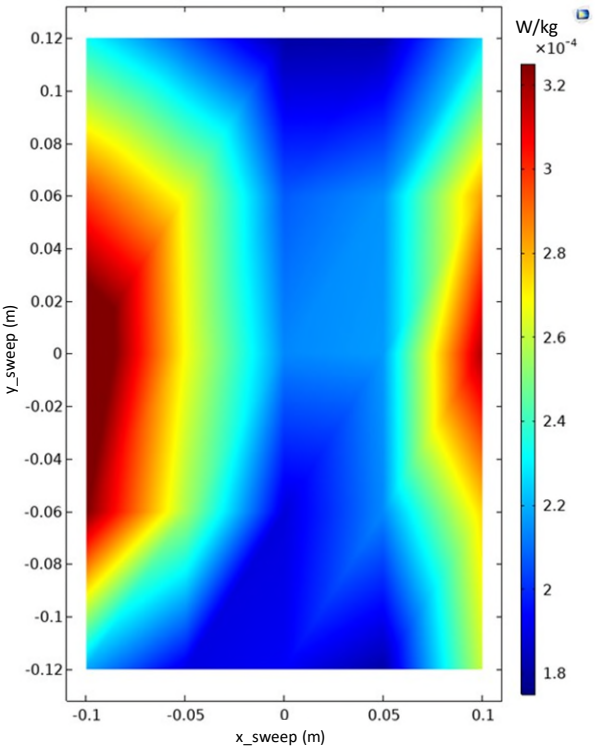

Figure 14: Worst case AED pad positioning on SAR heating. Using one electrode, the tissue peak temperature over the phantom was identified by moving the electrode location into 25 different pre-defined positions, i.e. by combining 5 transversal and 5 longitudinal positions in a regular grid. With x_sweep and y_sweep representing the location from the midpoint of the phantom to the midpoint of the electrode.

AED Pad SAR computation

Single electrode heating

After the prior determination of the AED pad location with the highest tissue heating, all following simulations were run with electrodes placed at the left centre side of the virtual phantom. Figure 15 shows the SAR distribution over the surface of the virtual phantom in normal conditions without any electrode and the distribution along a virtual phantom with a single AED electrode. Without electrode the highest peak SAR value is 0.23 x 10^{-4} W/kg. This pattern is comparable to the “worst case” simulation, as earlier described and presented (Figure 14). The plot with AED electrode in Figure 15 illustrates the computed local SAR values, revealing that SAR heating mainly occurs at the top and bottom edges of the AED pad. In this case the peak SAR value increased to 2.18 x 10^{-4} W/kg.

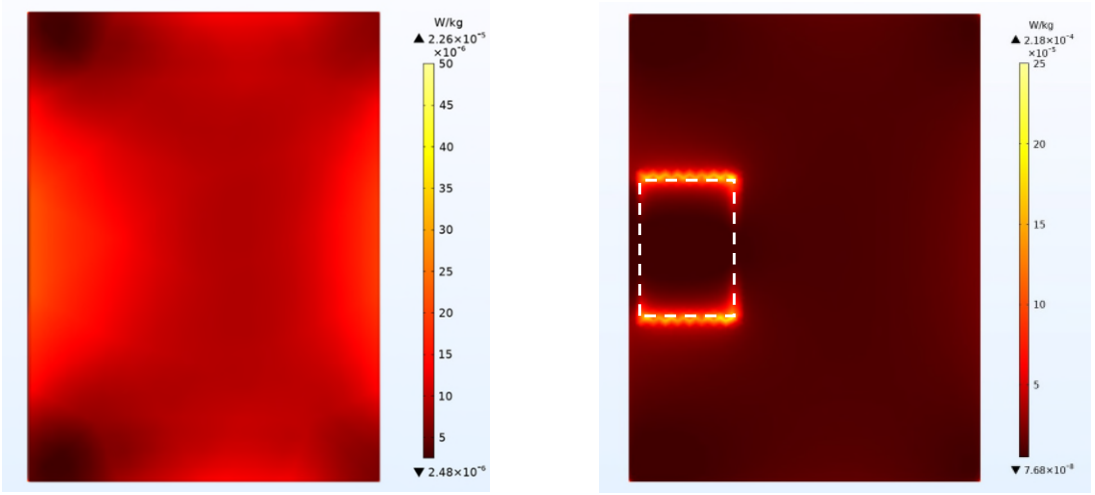

Figure 15: Phantom surface SAR heating. On the left; the usual process of tissue heating without any electrode, showing a maximal SAR value of 0.23 x 10^{-4} W/kg. On the right; the surface SAR values of the phantom with AED electrode, resulting in a higher peak SAR of 2.18 x 10^{-4} W/kg. Note: Color legend schemes are not comparable.

Multiple electrode heating

Based on theoretical assumptions, as described in the introduction chapter, size and numbers of AED pads ware altered in order to possibly achieve a decrease in SAR values. To break the influence of large odd conductive materials on field distribution and loops of eddy currents, the AED pads were split into different (two, four and six) parts. Because the highest SAR values are concentrated at the top and bottom edges of the AED pad, depending on the direction of the RF fields, a transversal or longitudinal split may also influence the outcome. Figure 16 shows a comparison of numbers of AED pads split in the transversal direction. Figure 17 demonstrates the SAR due to surface heating in the case of longitudinal positioning of the AED electrodes.

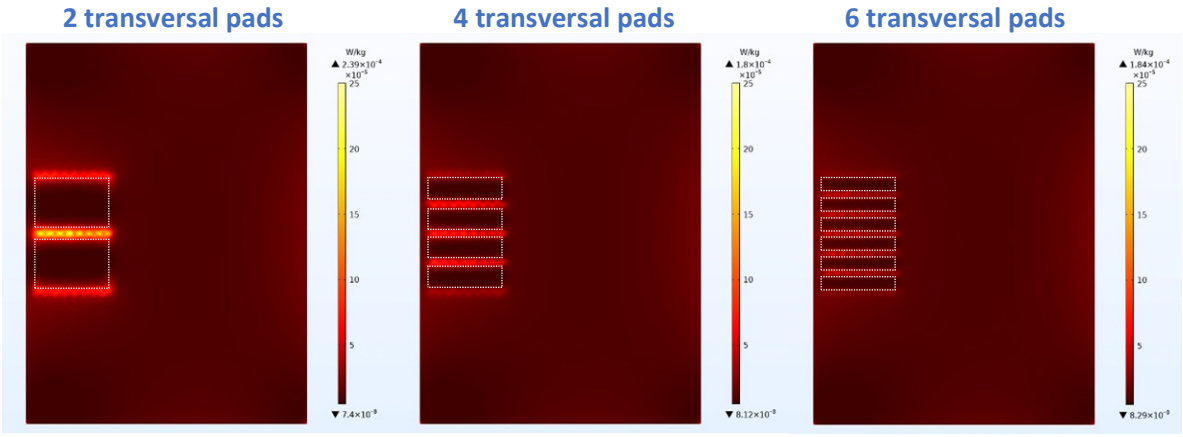

Figure 16: Transversal AED pad design. a) 2 parts. b) 4 parts. c) 6 parts. Simulation results showing considerable changes in SAR. For these transversal slits local SAR is decreasing with the amount of electrode parts.

Dividing the AED electrode in multiple transversal parts resulted in a spreading and decrease of SAR at the top and bottom of the total electrode. However, in between transversal electrode parts the SAR values of the opposite bottom and top edges are added together, so locally there are higher SAR values presented (Figure 16). Visually, the differences in SAR between the longitudinal two, four and six electrode parts in these simulations seem less obvious (Figure 17). The corresponding peak SAR values from both figures are presented in Table 1.

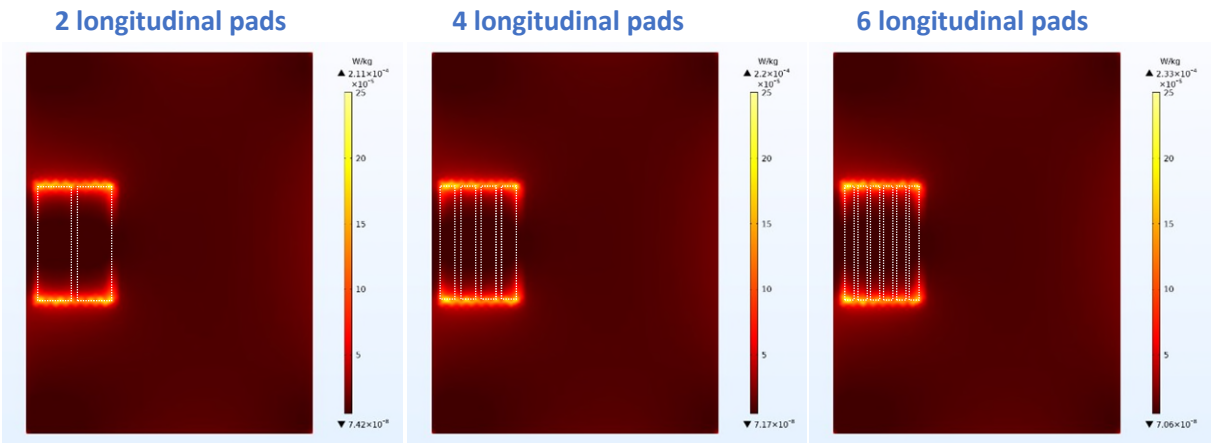

Figure 17: Longitudinal AED pad design. a) 2 parts. b) 4 parts. c) 6 parts. Simulation results showing hardy any changes in SAR over the increasing number of longitudinal electrode parts.

As can be seen from Table 1, a split into two parts does not necessarily result in a reduction of SAR. Figure 16a shows that between the two transversal parts the SAR values are added together, which ensures that higher values are found in this situation. Dividing the electrode in four and six parts will reduce the SAR values further, so the summed in-between SAR values will also diminish. This addition effect is irrelevant for the longitudinal parts, due to the direction of the RF currents (Figure 17). The SAR values in longitudinal split electrodes are comparable to those of one standard AED pad. Once again, the electrode parts closer to the coil show higher peak SAR values.

	No electrode	One electrode	Two electrode	Four electrodes	Six electrodes
Transversal split	0.23	2.18	2.39	1.80	1.84
Longitudinal split	0.23	2.18	2.11	2.20	2.33

Table 1: Peak SAR values from COMSOL simulations comparing a variety of AED pads expressed in W/kg (x 10^{-4}).

10-gram SAR distribution

For a better estimate of tissue temperature, the local 1-gram SAR values were converted into an average 10-gram SAR distribution within the total volume of the virtual phantom model. This results in a three dimensional matrix from which cross-sections were taken for the display. The layer with the maximal 10-gram SAR value was selected; apparently this was one of the first layers under the AED pad. Figure 18 shows these cross section models of the virtual phantom tissue with and without electrode. In Figure 19 and Figure 20 the 10-gram SAR averaging result of the splits in transversal and longitudinal direction are presented.

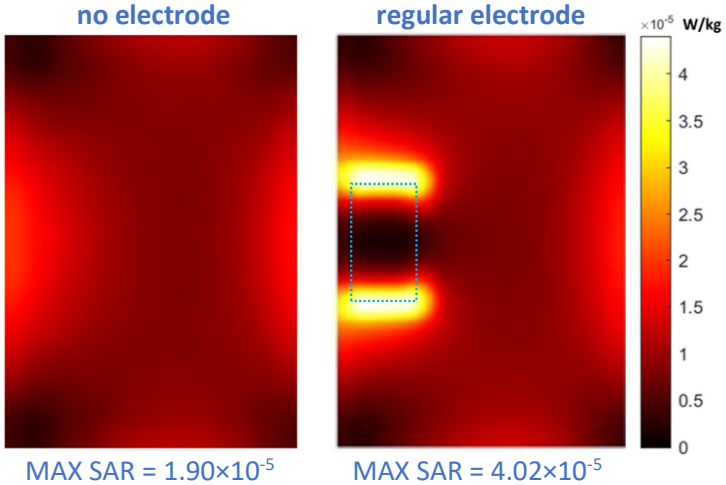

Figure 18: SAR 10-gram average values. It shows a cross-section of the top layer of the phantom. On the left; the 10-grams SAR averaging of only phantom tissue. On the right; the averaging result of the phantom with a regular electrode.

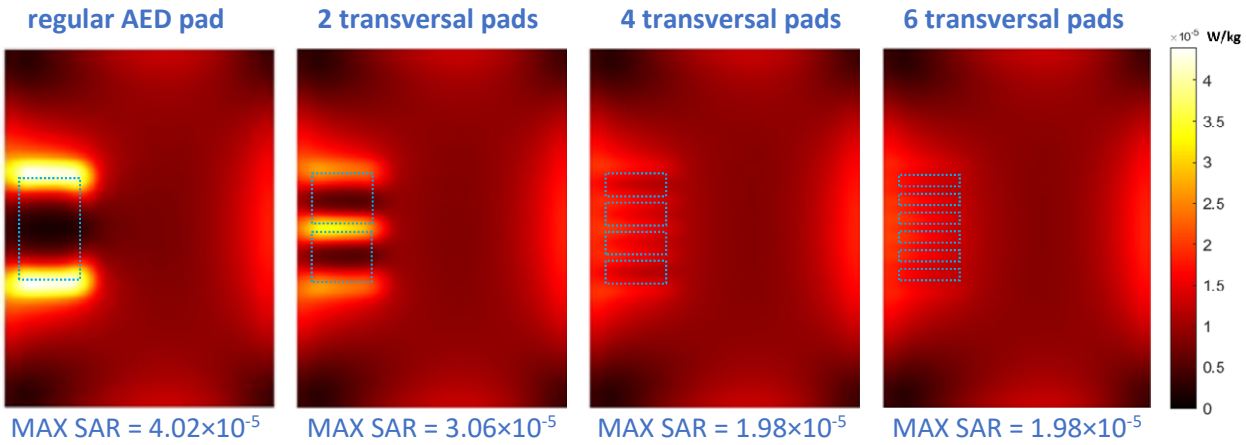

Figure 19: SAR 10-gram average values for transversal splits. It shows a cross-section of the top layer of the phantom. On the left starting with the regular electrode, then splitting it into multiple parts going to the right.

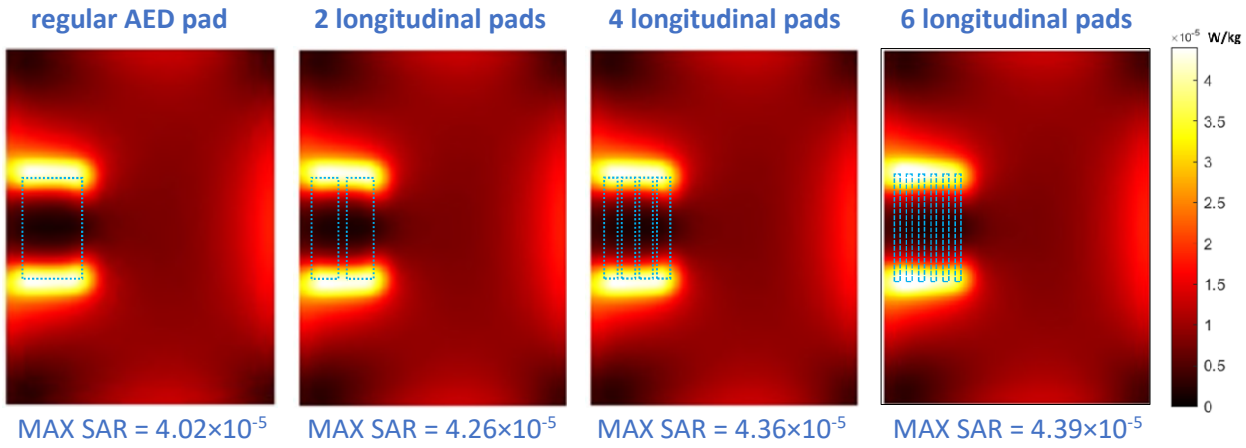

Figure 20: SAR 10-gram average values for longitudinal splits. It shows a cross-section at the top layer of the phantom. On the left starting with the regular electrode, then splitting it into multiple parts going to the right.

The 10 gram SAR peak values are presented in Table 2. Values decreased with higher numbers of electrodes when transversally split (from 4.02 to 1.98 W/kg (x 10^{-5})), although there seems to be no difference between four or six electrodes used. When electrodes were divided longitudinally a slight 10-gram SAR peak value increase with numbers of electrodes were seen (from 4.02 to 4.39 W/kg (x 10^{-5})). So splitting in a longitudinal way eliminates the beneficial effect of the application of several electrodes on tissue heating.

	one electrode	two electrode	Four electrodes	six electrodes
Transversal split	4.02	3.06	1.98	1.98
Longitudinal split	4.02	4.26	4.36	4.39

Table 2: Peak values of 10-gram SAR distribution from MATLAB computations comparing a variety of AED pads expressed in W/kg (x 10^{-5}).

In vitro experiment

The simulation setup computed with COMSOL was repeated in the clinical situation using the properties of the artificial AED electrodes and the phantom. Due to practical circumstance and availability of devices and materials minor adjustments were made. More specifically, the phantom used in the measurements (21 x 33 x 8 cm^3) was smaller than the phantom model used in the simulations (30 x 40 x 20 cm^3) and the AED pad had rounded instead of rectangular corners. This may have influenced the comparability of the absolute outcomes between the computer simulation and the in vitro experiment, but the general findings within the COMSOL computer simulation and the experiment respectively are consistent.

IR image processing

Figure 21 shows the difference in heat distribution over the whole surface of the phantom comparing post to pre MRI session. During an MRI application the phantom showed a moderate increase of the heat pattern and a 0.70 °C peak temperature rise. A single electrode revealed locations on top and the bottom with a peak temperature increase of 1.63 °C. Transversal splitting in two pads decreased the peak temperature difference to 1.41 °C. Separating the pad into four transversal parts diminished the peak temperature increase even more to 1.19 °C. Splitting into longitudinal AED parts had less effect on the adjacent tissue heating: peak temperatures increased by 2.16 °C and 2.51 °C with two and four parts, respectively. Transversal slits and splitting of the AED pads diminished the peak temperature rise, whereas splitting in a longitudinal plane enhanced the peak temperature, as expected based on the EM theory and the results from the computer simulation (see Figure 21 and Table 3). Remarkably, the flareups around the electrodes are more prominent at the left side, because this part of the phantom is closer to the RF coils, where logically the field is stronger, resulting in higher temperatures. The presence of an electrode creates higher eddy currents through the phantom and these current loops will return on the right side within the phantom, creating a temperature rise even when there is no electrode located. This may explain the flareups at the right side of the phantom in Figure 21.

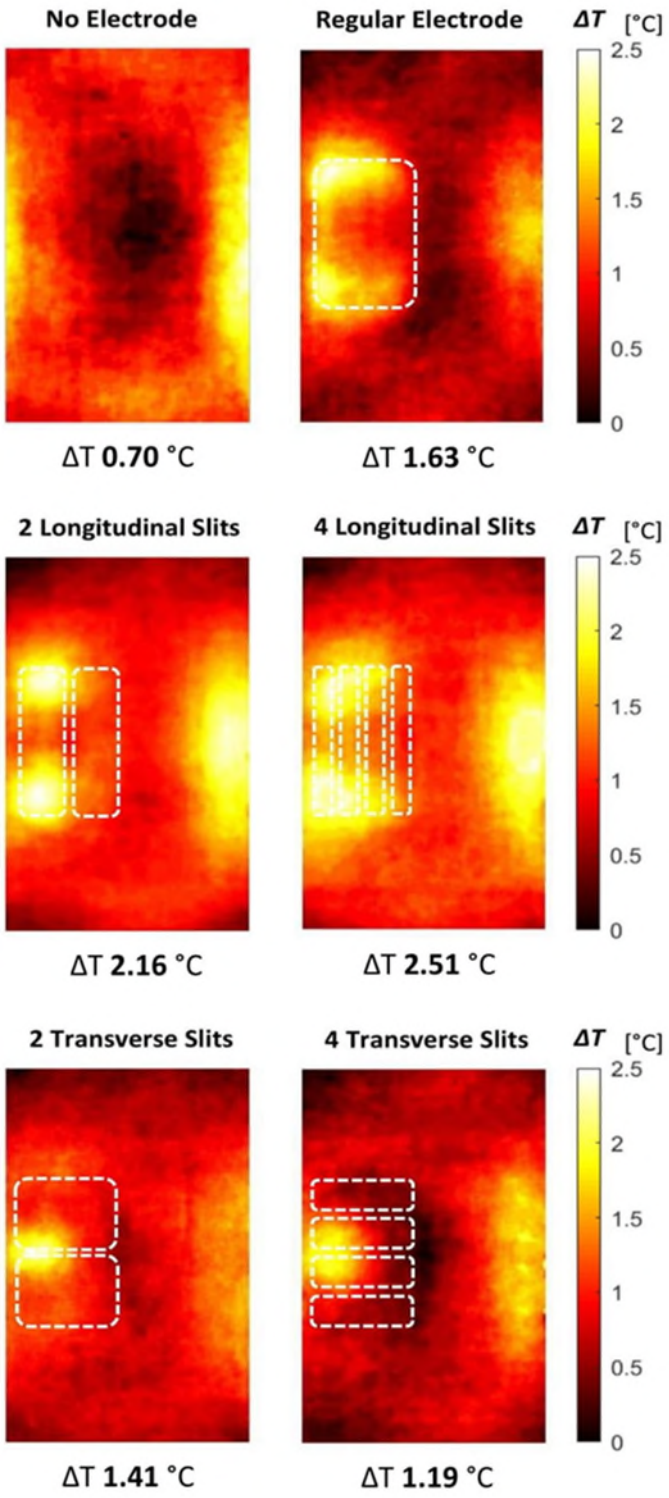

Figure 21: Thermographic images showing temperature increases in different defibrillation electrode configurations. RF heating was considerably higher when longitudinal slits were introduced and decreased for transversal slits.

	No electrode	One electrode	Two electrodes	Four electrodes
Transversal split	0.70	1.63	1.41	1.19
Longitudinal split	0.70	1.63	2.16	2.51

Table 3:Peak temperature increase during MRI expressed in °C.

Discussion

Comparability of computer simulation and in vitro experiment.

Both the COMSOL computer simulations and the in vitro experiments showed comparable results, concerning the alteration of SAR and tissue temperature during MRI sessions, the effect of positioning of the AED electrodes and the influence of the application of numerous electrodes. It should be noted, however, that due to practical limitations, the computer model had some minor differences as compared to the in vitro measurement setup. In the COMSOL model several series of computer simulations could be run. So, the effect of numerous AED pads from one to six could be studied and even simulations with more AED electrode would have been possible, but results revealed that further applications and investigation with more than six electrodes were unnecessary. Actually, peak SAR values and 10-gram SAR surface distribution hardly changed using four or six electrodes as can be seen from Tables 1 and 2. Therefore, the in vitro experiment in the MRI bore was limited to four electrodes under the assumption that an increase of numbers of AED pad would show similar outcomes. In fact, the findings from the computer simulation were used to specify the experimental design and improve validity of the comparison of outcomes between the simulations and the in vitro experiment.

In the in vitro experiment the clinically available standard AED pads of 8.5 x 12 cm^2 (approx. 85 cm^2) with rounded top and bottom were used (see Figure 12). For the computer simulation a simplification of the clinical AED pad geometry into straight angles was made to enable less complicated computations (see Figure 10). In the COMSOL model the AED pad was simulated as a metal plate of 8 cm by 12 cm (96 cm^2) with no thickness. Despite the small differences in surface area (approx. 10 cm^2), the obtained results from simulations and experiment measurements were comparable, because tissue heating appeared not to be effected by the size, but rather depended on the location and position of the AED electrode. However, in all cases especially adjacent to the upper and lower parts tissue heating occurred. The patterns of heating distribution obtained from the COMSOL simulations and the in vitro experiments were similar as can be seen from Figure 14 to Figure 21. From that perspective, in our opinion, computer simulations and the MRI experiments are in good agreement.

Validity of temperature measurements

We expect that subsequent measurements of the various AED slits in the MRI experiment may have influenced delta temperature ΔT (comparing before and after treatment) outcome. It was not practical to wait for the full cooling down to initial room temperatures of the phantom before starting the next measurement, because the MRI experiment time was strictly limited to a total of 3 hours. So initial temperatures of successive in vitro testing may have been increased slightly over time. Although delta temperatures ΔT are presented and therefore the effect of a slightly higher initial temperature was reduced, some kind of ceiling effect could have been present, especially in the latter experiments. Due to higher initial temperatures the measured temperature rise during MRI treatment may underestimate the actually expected temperature increase. However, the differences between mean initial temperatures were not substantial and varied marginally from 24.1 °C to 25.1 °C.

Comparison with published works

This study demonstrated that unwanted tissue heating adjacent to AED pads during MRI can be reduced by dividing the AED pads into smaller multiple parts, that are split in the transversal plane towards the RF direction of the MRI. Tissue heating under MRI was reduced from 1.63°C, to 1.41°C to finally 1.19°C, by using one, two or four electrodes each of smaller size, respectively. This is within the limits of guidelines of the IEC[32] that accept an increase of 1.5 °C. In other studies comparable figures of tissue heating were found.

Schmidt et al. studied tissue heating due to a newly developed MRI-conditional defibrillation system in healthy volunteers and animal subjects comprising four swine [23]. During an 11-minute continuous imaging experiment using the 4.4 W/kg steady-state free precession sequence, the mean peak temperature rise observed in swine beneath the defibrillation pads was 1.4 C°. The healthy volunteers' skin regions below the pads were examined at the end of the heating tests, and no burns were observed, nor were any sensations reported. The absolute skin temperatures of human volunteers were not presented. The main focus of the study was on the disturbance of the quality of the MRI picture when this novel device was used. However, findings were comparable with results from our study.

In a study by Shusterman et al. the feasibility and safety of in-bore defibrillation was investigated[33]. A total of 18 high-energy (200-360 J) defibrillation experiments were conducted in six anesthetised pigs on a 1.5 T MRI scanner outside the magnet bore, inside the bore, and during scanning, using adult and paediatric defibrillation pads. The mean temperature change under the defibrillation pads during a 6-minute 1.5 T MRI scan did not exceed 1 °C.

Additionally, further literature was searched using Pubmed, Sciencedirect, IEEE Xplore and SpringerLink with search terms: "MRI" AND "temperature" AND "external defibrillation", but mainly papers related to internal defibrillation devices and/or pacemakers were found. No further relevant studies, other than already cited in this thesis were found.

Clinical implications

The findings from the presented computer simulation study and in vitro experiments together with the few relevant other studies in animals and healthy human subjects are promising for future application of external defibrillation devices under MRI scanning. Unwanted tissue heating adjacent to the attached defibrillation electrodes can be prevented by dividing standard AED pads into at least four parts, transversally positioned to the RF direction. The extra heating caused by the AED pads does not exceed the safety limits of a maximal increase of 1.5 °C in European and international guidelines. Besides this, the quality of MRI pictures is not dramatically influenced by (multiple) external AED pads[23] [33]. For clinical practice these findings must be implemented in the defibrillation device that are already MRI compatible. However, dividing electrodes in several parts, spitting transversally does diminish unwanted tissue heating, but it is still unclear, although the total of the smaller parts have the same surface, if the power of defibrillation is clinically sufficient. Studies into this subject were not found, so this needs further verification in future research.

Further research

However, these novel equipment is not permissible clinically at this moment and development need further research, studying the effect of multiple pads and slit direction subsequently in vitro experiment, animals, healthy volunteers and eventually patients. Also the potential additional effect of wire connection to the AED pads and the possible adjacent heating along the wires must be investigated. Anticipating on that following research we already investigated, additionally to the initial research questions in this study, the effect of wiring the parts of the AED pad in the COMSOL simulation. Subsequently connecting wires at the left, in the middle and at the right of the AED pads respectively were studied in a simulation, with four electrode parts.

Wire connected AED electrodes

As appeared from the results, dividing the AED pad in four different parts showed the best reduction in peak SAR. Therefore, the findings of this extra added investigation with four wired electrode parts are visualised in Figure 22. A connecting wire at the left side induced the highest increase of adjacent tissue heating and calculated peak SAR, followed by the midpoint connection. A wire connection at the right side hardly revealed any increase compared to the simulation without wiring (1.80 vs 1.85 W/kg (x 10^{-4}). Apparently, the further away from the coil and closer to the centre point of the MRI, the strength of the RF field is decreasing, so the extra wiring has less impact on the redirection of the eddy currents that causes extra tissue heating (Figure 22). This extra COMSOL simulation with wired electrodes was performed for two, four and six electrode parts; The wiring effect on peak SAR values for each situation is presented in Table 4. It consistently shows the diminishing peak SAR figures from left to right wiring.

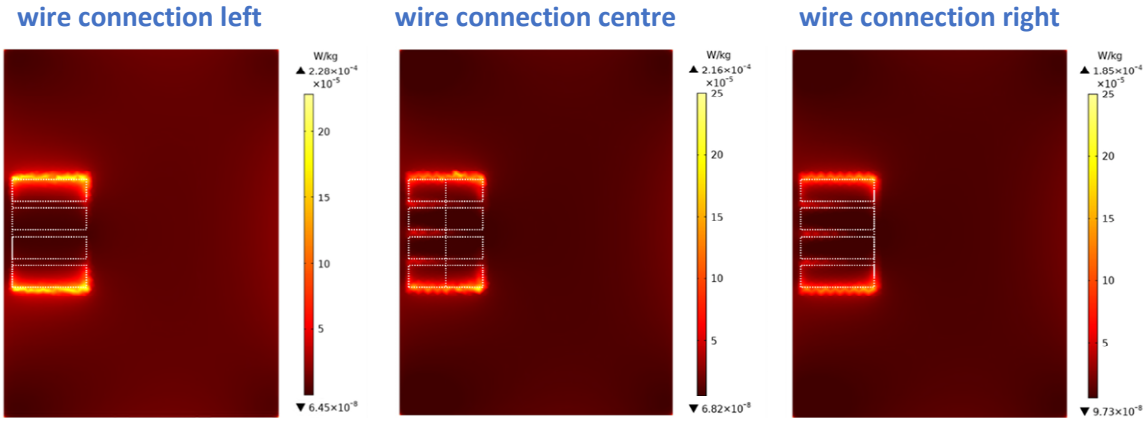

Figure 22: COMSOL simulation with vertical wire connection between the four transversal slits. Wire connection of the electrodes is completely left, at the midpoint and completely right (in images from left to right).

	one electrode	two electrode	Four electrodes	six electrodes
Transversal split	2.18	2.39	1.80	1.84
- connection left	2.18	2.32	2.28	2.20
- connection centre	2.18	2.32	2.16	1.96
- connection right	2.18	1.90	1.85	1.96

Table 4: Peak SAR values from COMSOL simulations comparing a variety of AED pads expressed in W/kg (x 10^{-4}).

Conclusions

In this paper we present computer simulation and in vitro experiments pertaining the RF safety of AED electrodes used during an in-bore defibrillation setup. The evaluation is based on the quantification of SAR values and temperature rise due to unwanted tissue heating. Using the simulated model, the "worst case" location, i.e. the location on the virtual phantom surface with highest tissue temperature increase due to MRI scanning, was determined. It was found that in the emulated left centre side of the virtual phantom model, a hotspot was observed because of the phase delay direction of the MRI coils. Due to this direction there are no energy losses of the magnetic field by going through the tissue on that site of the virtual phantom, which answers research question 1 stated above.

Using the position of the hotspot, further simulations revealed that by increasing number of AED pad parts, the adjacent tissue heating at top and bottom of the pad changed. Transversal splitting of one electrode into two, four and six parts substantially reduced peak SAR values from 2.18, to 2.39, 1.80 and 1.84 W/kg (x 10^{-4}), respectively answering research questions 2 and 3 outlined above. However, when the pad was split longitudinally the SAR slightly increased with the number of electrodes from 2.18 to 2.33 W/kg (x 10^{-4}), which addresses research question 3. The computed and 10-gram SAR peak values showed the same pattern, as expected.

The COMSOL simulation findings were confirmed by practical in vitro experiments with a phantom in the MRI coil. Again, significant tissue heating was seen at the top and bottom of the AED pads. In the setup with the transversal slits the ΔT peak temperature decreased from 1.63 to 1.19 °C, while with longitudinal slits a substantial increase of 0.88 °C (from 1.63 to 2.51 °C) was found, which addresses research questions 2 and 3.

In conclusion, adjacent unwanted tissue heating is prominent at the top and bottom of the AED pad, but can be reduced by the application of smaller and multiple parts of AED electrodes, that are split in the transversal plane compared to the field direction of the MRI.

References

1. El Hajj SC, Gold MR. Magnetic Resonance Imaging-Conditional External Cardiac Defibrillator: Expanding Access and Safety During Magnetic Resonance Imaging. LID - e005573 [pii] FAU - El Hajj, Stephanie C. 2016(1942-0080 (Electronic))
2. Winter L, Seifert F, Zilberti L, et al. MRI-Related Heating of Implants and Devices: A Review. *J Magn Reson Imaging* 2021;53(6):1646-65. doi: 10.1002/jmri.27194 [published Online First: 20200526]
3. Buchli R, Boesiger P, Meier D. Heating effects of metallic implants by MRI examinations. *Magn Reson Med* 1988;7(3):255-61. doi: 10.1002/mrm.1910070302
4. Arduino A, Zanovello U, Hand J, et al. Heating of hip joint implants in MRI: The combined effect of RF and switched-gradient fields. *Magn Reson Med* 2021;85(6):3447-62. doi: 10.1002/mrm.28666 [published Online First: 20210122]
5. Iwatsuki K, Yoneda H, Onishi T, et al. Compatibility of magnetic resonance imaging in patients with orthopedic implants: manufacturer questionnaires. *Nagoya J Med Sci* 2020;82(1):79-84. doi: 10.18999/nagjms.82.1.79
6. Bryant M. MRI Safety: An Update Applied Radiology: the journal of practical medical imaging and management2021 [updated 08-2021. Available from: https://www.appliedradiology.com/communities/MR-Community/mri-safety-an-update.
7. Serai SD, Ho ML, Artunduaga M, et al. Components of a magnetic resonance imaging system and their relationship to safety and image quality. *Pediatr Radiol* 2021;51(5):716-23. doi: 10.1007/s00247-020-04894-9 [published Online First: 20210419]
8. AD Elster EL. Questions and answers in MRI 2021 [Available from: https://mriquestions.com/.
9. Kanal E. Standardized Approaches to MR Safety Assessment of Patients with Implanted Devices. *Magn Reson Imaging Clin N Am* 2020;28(4):537-48. doi: 10.1016/j.mric.2020.07.003 [published Online First: 20200918]
10. Currie S, Hoggard N, Craven IJ, et al. Understanding MRI: basic MR physics for physicians. *Postgrad Med J* 2013;89(1050):209-23. doi: 10.1136/postgradmedj-2012-131342 [published Online First: 20121207]
11. Ridgway JP. Cardiovascular magnetic resonance physics for clinicians: part I. *J Cardiovasc Magn Reson* 2010;12:71. doi: 10.1186/1532-429X-12-71 [published Online First: 20101130]
12. Berger A. Magnetic resonance imaging. *BMJ* 2002;324(7328):35-35. doi: 10.1136/bmj.324.7328.35
13. FEM Based design and simulation tool for MRI birdcage coils Including eigenfrequency analysis; 2012.
14. Hayes CE, Edelstein WA, Schenck JF, et al. An efficient, highly homogeneous radiofrequency coil for whole-body NMR imaging at 1.5 T. *Journal of Magnetic Resonance* 1985;63:622-28.
15. Miklavčič D, Pavšelj N, Hart FX. Electric Properties of Tissues. Wiley Encyclopedia of Biomedical Engineering2006.
16. Badea E, Craiu O. Eddy current effects in MRI superconducting magnets. *Magnetics, IEEE Transactions on* 1997;33:1330-33. doi: 10.1109/20.582501
17. Yetisir F. Local and global SAR constrained large tip angle 3D kT-points parallel transmit pulse design at 7 T. 2014
18. Hirata A, Fujiwara O. The correlation between mass-averaged SAR and temperature elevation in the human head model exposed to RF near-fields from 1 to 6 GHz. *Phys Med Biol* 2009;54(23):7227-38. doi: 10.1088/0031-9155/54/23/013 [published Online First: 20091117]
19. ASTM I. Standard practice for marking medical devices and other items for safety in the magnetic resonance environment. *ASTM f2503-13* 2014
20. Dempsey MF, Condon B, Hadley DM. Investigation of the factors responsible for burns during MRI. *J Magn Reson Imaging* 2001;13(4):627-31. doi: 10.1002/jmri.1088

21. Oster J, Clifford GD. Acquisition of electrocardiogram signals during magnetic resonance imaging. 2017(1361-6579 (Electronic))
22. Shinbane JS, Colletti PM, Shellock FG. Magnetic resonance imaging in patients with cardiac pacemakers: era of "MR Conditional" designs. *J Cardiovasc Magn Reson* 2011;13(1):63-63. doi: 10.1186/1532-429X-13-63
23. Schmidt EJ, Watkins RD, Zviman MM, et al. A Magnetic Resonance Imaging-Conditional External Cardiac Defibrillator for Resuscitation Within the Magnetic Resonance Imaging Scanner Bore. LID - e005091. 2016(1942-0080 (Electronic))
24. Kroll MW, Fish Rm Fau - Calkins H, Calkins H Fau - Halperin H, et al. Defibrillation success rates for electrically-induced fibrillation: hair of the dog. 2012(2694-0604 (Electronic))
25. Tse ZT, Dumoulin Cl Fau - Clifford GD, Clifford Gd Fau - Schweitzer J, et al. A 1.5T MRI-conditional 12-lead electrocardiogram for MRI and intra-MR intervention. 2014(1522-2594 (Electronic))
26. Krug JW, Rose G, Clifford GD, et al. ECG-based gating in ultra high field cardiovascular magnetic resonance using an independent component analysis approach. *J Cardiovasc Magn Reson* 2013;15:104. doi: 10.1186/1532-429X-15-104 [published Online First: 20131119]
27. Kligfield P Fau - Gettes LS, Gettes Ls Fau - Bailey JJ, Bailey Jj Fau - Childers R, et al. Recommendations for the standardization and interpretation of the electrocardiogram. Part I: The electrocardiogram and its technology. A scientific statement from the American Heart Association Electrocardiography and Arrhythmias Committee, Council on Clinical Cardiology; the American College of Cardiology Foundation; and the Heart Rhythm Society. 2007(1547-5271 (Print))
28. Bækgaard JS, Viereck S, Møller TP, et al. The Effects of Public Access Defibrillation on Survival After Out-of-Hospital Cardiac Arrest: A Systematic Review of Observational Studies. 2017(1524-4539 (Electronic))
29. Dalzell GW, Cunningham Sr Fau - Anderson J, Anderson J Fau - Adgey AA, et al. Electrode pad size, transthoracic impedance and success of external ventricular defibrillation. 1989(0002-9149 (Print))
30. Frankel J, Hansson Mild K, Olsrud J, et al. EMF exposure variation among MRI sequences from pediatric examination protocols. *Bioelectromagnetics* 2019;40(1):3-15. doi: 10.1002/bem.22159 [published Online First: 20181130]
31. FDA. Criteria for Significant Risk Investigations of Magnetic Resonance Diagnostic Devices. White Oak, Md: Food and Drug Administration, 2014.
32. IEC. International Electrotechnical Commission 60601-2-33. Medical electrical equipment - Part 2: Particular requirements for the basic safety and essential performance of magnetic resonance equipment for medical diagnosis; 2-33, 2010.
33. Shusterman V, Hodgson-Zingman D, Thedens D, et al. High-energy external defibrillation and transcutaneous pacing during MRI: feasibility and safety. *Journal of Cardiovascular Magnetic Resonance* 2019;21(1):47. doi: 10.1186/s12968-019-0558-z
34. Anzai Y, Moy L. Point-of-Care Low-Field-Strength MRI Is Moving Beyond the Hype. *Radiology* 2022:221278. doi: 10.1148/radiol.221278 [published Online First: 20220802]
35. Liu W, Collins CM, Smith MB. Calculations of B1 Distribution, Specific Energy Absorption Rate, and Intrinsic Signal-to-Noise Ratio for a Body-Size Birdcage Coil Loaded with Different Human Subjects at 64 and 128 MHz. *Appl Magn Reson* 2005;29(1):5-18. doi: 10.1007/BF03166953
36. Ghodgaonkar DK, Gandhi OP, Iskander MF. Complex permittivity of human skin in vivo in the frequency band 26.5-60 GHz. *IEEE Antennas and Propagation Society International Symposium Transmitting Waves of Progress to the Next Millennium 2000 Digest Held in conjunction with: USNC/URSI National Radio Science Meeting (C* 2000;2:1100-03 vol.2.
37. Jaehoon Kim and Rahmat-Samii Y. SAR reduction of implanted planar inverted F antennas with non-uniform width radiator, 2006:1091-94.
38. Grekov AN, Grekov NA, Sychov EN. Measuring Salinity and Density of Seawater Samples with Different Salt Compositions and Suspended Materials. *Metrology* 2021;1(2):107-21.

39. Yu Z, Xin X, Collins CM. Potential for high-permittivity materials to reduce local SAR at a pacemaker lead tip during MRI of the head with a body transmit coil at 3 T. *Magn Reson Med* 2017;78(1):383-86. doi: 10.1002/mrm.26344 [published Online First: 20161007]
40. Klaessens J, van der Veen A, Verdaasdonk R. Comparison of the temperature accuracy between smart phone based and high-end thermal cameras using a temperature gradient phantom: SPIE 2017:PWB.

Appendix A

```
clear; close all; clc;

rho = 1000;     % volumetric mass density [kg/m3]
mtarget = 0.01; % 10g target averaging mass
TOL = 0.001;    % 1g accuracy

%data_in = importdata('SARexport_elc6_grid4.txt',' ',14);
data_in = importdata('MRI_SARgrid_H2.txt',' ',14);

%% import data
x = str2num(data_in.textdata{10});
y = str2num(data_in.textdata{11});
z = str2num(data_in.textdata{12});
dV = mean(diff(x))*mean(diff(y))*mean(diff(z)); % voxel volume

SAR = permute(reshape(data_in.data,[length(y) length(z) length(x)]),[3 2 1]);
SARlim = [0 1]*max(SAR(:))*0.5;

%% plots

figure(1); set(gcf,'Position',[150 500 1100 350]); colormap(hot);
subplot(2,3,1); imagesc(squeeze(SAR(:,:,208)),SARlim); axis image xy off;
subplot(2,3,2); imagesc(squeeze(SAR(:,200,:)),SARlim); axis image xy off; title('SAR cross
section');
subplot(2,3,3); imagesc(squeeze(SAR(160,:,:)),SARlim); axis image xy off;
subplot(2,3,4); imagesc(squeeze(max(SAR,[],3)),SARlim); axis image xy off;
subplot(2,3,5); imagesc(squeeze(max(SAR,[],2)),SARlim); axis image xy off; title('SAR MIP');
subplot(2,3,6); imagesc(squeeze(max(SAR,[],1)),SARlim); axis image xy off;

%% average SAR data
m = dV*rho*ones(size(SAR)); % mass array
[SAR10,err] = genSARav(SAR,m,mtarget,50,TOL);
SAR10lim = [0 1]*max(SAR10(:));

figure(2); set(gcf,'Position',[150 500 1100 350]); colormap(hot);
subplot(2,3,1); imagesc(squeeze(SAR10(:,:,208)),SAR10lim); axis image xy off;
subplot(2,3,2); imagesc(squeeze(SAR10(:,200,:)),SAR10lim); axis image xy off; title('10g SAR
cross section');
subplot(2,3,3); imagesc(squeeze(SAR10(160,:,:)),SAR10lim); axis image xy off;
subplot(2,3,4); imagesc(squeeze(max(SAR10,[],3)),SAR10lim); axis image xy off;
subplot(2,3,5); imagesc(squeeze(max(SAR10,[],2)),SAR10lim); axis image xy off; title('10g SAR
MIP');
subplot(2,3,6); imagesc(squeeze(max(SAR10,[],1)),SAR10lim); axis image xy off;
```

Appendix B

```
function [SARav,error,r] = genSARav(SAR,m,mtarget,maxiter,TOL,varargin)

%
% [SARav,error,r] = gen_SARav(SAR,m,mtarget,maxiter,TOL,displayflag,rseq)
%
% Generate averaged SAR using the kernel-growing FFT method.
%
% m denotes the 3D mass array in kg
%

%% INITIALIZATION
fftsize = 2.^nextpow2(size(m));
mask = false(fftsize);
mask(1:size(m,1),1:size(m,2),1:size(m,3)) = m~=0;
[X,Y,Z] = ndgrid(-fftsize(1)/2+1:fftsize(1)/2,-fftsize(2)/2+1:fftsize(2)/2,-
fftsize(3)/2+1:fftsize(3)/2);
R = circshift(sqrt(X.^2 + Y.^2 + Z.^2),fftsize/2+1); % distance array for generating the
circular averaging kernel

%% SETUP SERIES OF KERNEL RADII
rmin = nthroot(3/(4*pi)*mtarget/max(nonzeros(m)),3);
rmean = nthroot(3/(4*pi)*mtarget/mean(nonzeros(m)),3);  % based on mean mass
rmax = nthroot(3/(4*pi)*mtarget/min(nonzeros(m)),3);
r = zeros(1,maxiter);
if (nargin==7)&&~isempty(varargin{2})    % use pre-defined sequence of kernel sizes
    maxiter = length(varargin{2});
    r(1:length(varargin{2})) = varargin{2};
else
    factor = [0.9 0.95 0.975 1 1.025 1.05 1.1 1.2 1.3 1.4 1.7 2.3 3];
    r(1:(length(factor)+1)) = [rmin rmean*factor];
end

%% INITIALIZE DISPLAY (OPTIONAL)
if (nargin>=6)&&varargin{1}
    figure(100); set(gcf,'Position',[50 100 800 375]); ziso = round(size(m,3)/2); yiso =
round(size(m,2)/2);
    subplot(2,4,1); h(1) = imagesc(zeros(size(m,1),size(m,2)).',[0 1.1]*mtarget); axis image
xy off; title('Averaged mass');
    subplot(2,4,2); h(2) = imagesc(zeros(size(m,1),size(m,2)).',[0 1.1]*mtarget); axis image
xy off; title('Mass error [g] (MIP)');
    subplot(2,4,3); h(3) = imagesc(zeros(size(m,1),size(m,2)).',[rmin rmax*1.1]); axis image
xy off; title('Radius used');
    subplot(2,4,4); h(4) = imagesc(zeros(size(m,1),size(m,2)).'); axis image xy off;
title('Averaged data');
    subplot(2,4,5); h(5) = imagesc(zeros(size(m,1),size(m,3)).',[0 1.1]*mtarget); axis image
xy off;
    h(60) = subplot(2,4,6); h(6) = imagesc(zeros(size(m,1),size(m,3)).',[0 1.1]*mtarget); axis
image xy off;
    subplot(2,4,7); h(7) = imagesc(zeros(size(m,1),size(m,3)).',[rmin rmax*1.1]); axis image
xy off;
    subplot(2,4,8); h(8) = imagesc(zeros(size(m,1),size(m,3)).'); axis image xy off;

    figure(101); set(gcf,'position',[900 100 500 375]);
    h(11) = subplot(2,2,1); title('Radii');
    h(12) = subplot(2,2,2); title('Maximum mass error [g]');
    h(13) = subplot(2,2,3); title('Mass histogram [g]');
    h(14) = subplot(2,2,4); title('Radii histogram');
    drawnow;

    disp(['Rmin = ' num2str(round(rmin,2)) '; Rmean = ' num2str(round(rmean,2)) '; Rmax = '
num2str(round(rmax,2))]);
end

%% KERNEL ITERATION LOOP
error = zeros(1,maxiter);
maskupdate = false(fftsize);
Rfinal = zeros(fftsize);
mfinal = zeros(fftsize);
SARav = zeros(fftsize,'like',SAR);
SARfft = fftn(SAR,fftsize);
mfft = fftn(m,fftsize);
maskfft = fftn(mask,fftsize);

for index = 1:maxiter
    kernel = interp1([-eps r(index)-0.5 r(index)+0.5 1e9],[1 1 0 0],R); % construct spherical
averaging kernel
    kernel = fftn(kernel,fftsize);
```

```
    mav = real(ifftn(kernel.*mfft,fftsize));          % local averaged mass

    maskupdate(mask) = abs(mav(mask)-mtarget)<abs(mfinal(mask)-mtarget);  % region to be
updated
    mfinal(maskupdate) = mav(maskupdate);       % final averaged mass
    Rfinal(maskupdate) = r(index);              % final averaging radius

    [error(index),I] = max(abs(mfinal(:)-mtarget).*mask(:));  % find voxel with maximum mass
error

    if nnz(maskupdate)>0                        % when updates are found
        Vav = real(ifftn(kernel.*maskfft,fftsize));   % local averaged volume
        temp = real(ifftn(kernel.*SARfft,fftsize));
        SARav(maskupdate) = temp(maskupdate)./Vav(maskupdate);  % update averaged SAR
    end

    if (nargin>=6)&&varargin{1}   % optional display
        disp(['Iteration ' num2str(index) ': radius = ' num2str(round(r(index),2)) '; error =
' num2str(round(error(index)*1000,3)) ' g']);

        set(100,'Name',['Iteration = ' num2str(index) '; r = '
num2str(round(r(index)*100)/100)]);
        set(h(1),'CData',mfinal(1:size(m,1),1:size(m,2),ziso).');

set(h(2),'CData',max(mask(1:size(m,1),1:size(m,2),:).*abs(mfinal(1:size(m,1),1:size(m,2),:)-
mtarget),[],3).');
        set(h(3),'CData',Rfinal(1:size(m,1),1:size(m,2),ziso).');
        set(h(4),'CData',SARav(1:size(m,1),1:size(m,2),ziso).');
        set(h(5),'CData',squeeze(mfinal(1:size(m,1),yiso,1:size(m,3))).');

set(h(6),'CData',squeeze(max(mask(1:size(m,1),:,1:size(m,3)).*abs(mfinal(1:size(m,1),:,1:size(
m,3))-mtarget),[],2)).'); title(h(60),['max error = ' num2str(round(max(abs(mfinal(mask)-
mtarget))*1e3,1)) ' g']);
        set(h(7),'CData',squeeze(Rfinal(1:size(m,1),yiso,1:size(m,3))).');
        set(h(8),'CData',squeeze(SARav(1:size(m,1),yiso,1:size(m,3))).');

        plot(h(11),nonzeros(r),'b*'); axis(h(11),[0 maxiter 0 ceil(max(r)*1.1)]);
title(h(11),'Radii');
        plot(h(12),1:index,error(1:index)*1e3,'b',[0 maxiter],[1 1]*TOL*1e3,'r--');
axis(h(12),[0 maxiter 0 error(1)*1.1*1e3]); title(h(12),'Maximum averaging error [g]');
        histogram(h(13),mfinal(mask)*1e3,(0:0.01:2)*mtarget*1e3); xlim(h(13),[0.5
1.5]*mtarget*1e3); title(h(13),'Mass histogram [g]');
        histogram(h(14),Rfinal(mask),rmin:(rmax*0.2-rmin)/2000:rmax*0.2); xlim(h(14),[0
rmax*0.2]); title(h(14),'Radii histogram');

        drawnow;
    end

    if (error(index)<TOL)||(index==maxiter)
        break
    elseif r(index+1)==0
        r(index+1) = nthroot(mtarget/(mfinal(I)+eps),3)*Rfinal(I);
        if r(index+1)<0.5   % minimum averaging kernel size of one voxel
            r(index+1) = 0.5;
        end
        if any(r(1:index)==r(index+1))  % take random radius when suggested radius has been
visited already
            r(index+1) = (0.5+rand)*r(index+1);
        end
    end
end

SARav = SARav(1:size(SAR,1),1:size(SAR,2),1:size(SAR,3));
error = error(1:index);
r = r(1:index);
```

Appendix C

```
%% video to frame ========================================================
v = VideoReader('AED1.MOV');
totalFrames = v.NumberOfFrames;
NFP = ceil(sqrt(totalFrames));
for i=1:totalFrames
frame = read(v,i);

% save frames
    if i == 127;
        ImgName = 'AED-T0.tif';
        imwrite(frame, ImgName);
    elseif i == 245;
        ImgName = 'AED-T1.tif';
        imwrite(frame, ImgName);
    end
end
v = VideoReader('AED2.MOV');
totalFrames = v.NumberOfFrames;
NFP = ceil(sqrt(totalFrames));
for i=1:totalFrames
frame = read(v,i);

% save frames
    if i == 61;
        ImgName = 'AED-TH2.tif';
        imwrite(frame, ImgName);
    end
end


v = VideoReader('AED3.MOV');
totalFrames = v.NumberOfFrames;
NFP = ceil(sqrt(totalFrames));
for i=1:totalFrames
frame = read(v,i);

% save frames
    if i == 48;
        ImgName = 'AED-TV2.tif';
        imwrite(frame, ImgName);
    elseif i == 110;
        ImgName = 'AED-TV4.tif';
        imwrite(frame, ImgName);
    elseif i == 177;
        ImgName = 'AED-TH4.tif';
        imwrite(frame, ImgName);
    end
end

%% image croping ==========================================================
baseFileName = 'AED-T0.tif';
folder = pwd;
fullFileName = fullfile(folder, baseFileName);
T0 = imread(fullFileName);
T0 = imcrop(T0,[90 75 300 500]);

baseFileName = 'AED-T1.tif';
folder = pwd;
fullFileName = fullfile(folder, baseFileName);
T1 = imread(fullFileName);
T1 = imcrop(T1,[90 75 300 500]);

baseFileName = 'AED-TH2.tif';
folder = pwd;
fullFileName = fullfile(folder, baseFileName);
TH2 = imread(fullFileName);
TH2 = imcrop(TH2,[90 75 300 500]);

baseFileName = 'AED-TH4.tif';
folder = pwd;
fullFileName = fullfile(folder, baseFileName);
TH4 = imread(fullFileName);
TH4 = imcrop(TH4,[90 75 300 500]);

baseFileName = 'AED-TV2.tif';
folder = pwd;
fullFileName = fullfile(folder, baseFileName);
```

```
TV2 = imread(fullFileName);
TV2 = imcrop(TV2,[90 75 300 500]);

baseFileName = 'AED-TV4.tif';
folder = pwd;
fullFileName = fullfile(folder, baseFileName);
TV4 = imread(fullFileName);
TV4 = imcrop(TV4,[90 75 300 500]);

%% substractions ============================================================

T0g=rgb2gray(T1);
T1g=rgb2gray(T1-T0);
TV2g=rgb2gray(TV2-TH2);
TV4g=rgb2gray(TV4-TV2);
TH2g=rgb2gray(TH2-T1);
TH4g=rgb2gray(TH4-TV4);

T0max = max(T0(:));
T1max = max(T1(:));
TV2max = max(TV2(:));
TV4max = max(TV4(:));
TH2max = max(TH2(:));
TH4max = max(TH4(:));

T0min = min(T0(:));
T1min = min(T1(:));
TV2min = min(TV2(:));
TV4min = min(TV4(:));
TH2min = min(TH2(:));
TH4min = min(TH4(:));

T0mean = mean(T0(:))/31.875+20;
T1mean = mean(T1(:))/31.875+20;
TV2mean = mean(TV2(:))/31.875+20;
TV4mean = mean(TV4(:))/31.875+20;
TH2mean = mean(TH2(:))/31.875+20;
TH4mean = mean(TH4(:))/31.875+20;

T0delta = (T0max-T0min);
T1delta = (T1max-T1min);
TH2delta = (TH2max-TH2min);
TV2delta = (TV2max-TV2min);
TH4delta = (TH4max-TH4min);
TV4delta = (TV4max-TV4min);

T0s  = T0*1 - T0*0.68;
T1s  = T1*1 - T0*0.68;
TH2s = TH2*1 - T1*0.68;
TH4s = TH4*1 - TV4*0.68;
TV2s = TV2*1 - TH2*0.68;
TV4s = TV4*1 - TV2*0.68;

%SubtractedImage = double(T1c) - double(T0c);
%T1min0 = imshow(SubtractedImage, []);

%% colorbar ================================================================
indexedImage = imgaussfilt(rgb2gray(T1),2);
highTemp = 28;
lowTemp = 20;
thermalImage = lowTemp + (highTemp - lowTemp) * mat2gray(indexedImage);
subplot(2, 5, 1);
%thermalImage = hot(thermalImage);
imshow(thermalImage, []);
colormap('hot');
colorbar;
title('WITH AED PAD');
hp = impixelinfo();
hp.Units = 'normalized';
hp.Position = [0.45, 0.03, 0.25, 0.05];

indexedImage = imgaussfilt(rgb2gray(TV2),2);
highTemp = 28;
lowTemp = 20;
thermalImage = lowTemp + (highTemp - lowTemp) * mat2gray(indexedImage);
subplot(2, 5, 2);
imshow(thermalImage, []);
colormap('hot');
colorbar;
```

```
title('Vertical 2 part AED');
hp = impixelinfo();
hp.Units = 'normalized';
hp.Position = [0.45, 0.03, 0.25, 0.05];

indexedImage = imgaussfilt(rgb2gray(TV4),2);
highTemp = 28;
lowTemp = 20;
thermalImage = lowTemp + (highTemp - lowTemp) * mat2gray(indexedImage);
subplot(2, 5, 3);
imshow(thermalImage, []);
colormap('hot');
colorbar;
title('Vertical 4 part AED');
hp = impixelinfo();
hp.Units = 'normalized';
hp.Position = [0.45, 0.03, 0.25, 0.05];

indexedImage = imgaussfilt(rgb2gray(TH2),2);
highTemp = 28;
lowTemp = 20;
thermalImage = lowTemp + (highTemp - lowTemp) * mat2gray(indexedImage);
subplot(2, 5, 4);
imshow(thermalImage, []);
colormap('hot');
colorbar;
title('Horizontal 2 part AED');
hp = impixelinfo();
hp.Units = 'normalized';
hp.Position = [0.45, 0.03, 0.25, 0.05];

indexedImage = imgaussfilt(rgb2gray(TH4),2);
highTemp = 28;
lowTemp = 20;
thermalImage = lowTemp + (highTemp - lowTemp) * mat2gray(indexedImage);
subplot(2, 5, 5);
imshow(thermalImage, []);
colormap('hot');
colorbar;
title('Horizontal 4 part AED');
hp = impixelinfo();
hp.Units = 'normalized';
hp.Position = [0.45, 0.03, 0.25, 0.05];

%% substractions
indexedImage = imgaussfilt(rgb2gray(T0s),1);
highTemp = 2.5;
lowTemp = 0;
thermalImage = lowTemp + (highTemp - lowTemp) * mat2gray(indexedImage);
subplot(2, 3, 1);
imshow(thermalImage, []);
colormap('hot');
colorbar;
title('No Electrode');
max(thermalImage(:));
hp = impixelinfo();
hp.Units = 'normalized';
hp.Position = [0.45, 0.03, 0.25, 0.05];
imgT0mean = mean(thermalImage(:))

indexedImage = imgaussfilt(rgb2gray(T1s),1);
highTemp = 2.5;
lowTemp = 0;
thermalImage = lowTemp + (highTemp - lowTemp) * mat2gray(indexedImage);
subplot(2, 3, 4);
imshow(thermalImage, []);
colormap('hot');
colorbar;
title('Regular Electrode');
max(thermalImage(:));
hp = impixelinfo();
hp.Units = 'normalized';
hp.Position = [0.45, 0.03, 0.25, 0.05];
ImgT1mean = mean(thermalImage(:))

indexedImage = imgaussfilt(rgb2gray(TV2s),1);
highTemp = 2.5;
lowTemp = 0;
thermalImage = lowTemp + (highTemp - lowTemp) * mat2gray(indexedImage);
```

```
subplot(2, 3, 2);
imshow(thermalImage, []);
colormap('hot');
colorbar;
title('2 Longitudinal Slits');
hp = impixelinfo();
hp.Units = 'normalized';
hp.Position = [0.45, 0.03, 0.25, 0.05];
ImgTV2mean = mean(thermalImage(:))

indexedImage = imgaussfilt(rgb2gray(TV4s),1);
highTemp = 2.5;
lowTemp = 0;
thermalImage = lowTemp + (highTemp - lowTemp) * mat2gray(indexedImage);
subplot(2, 3, 5);
imshow(thermalImage, []);
colormap('hot');
colorbar;
title('4 Longitudinal Slits');
hp = impixelinfo();
hp.Units = 'normalized';
hp.Position = [0.45, 0.03, 0.25, 0.05];
ImgTV4mean = mean(thermalImage(:))

indexedImage = imgaussfilt(rgb2gray(TH2s),1);
highTemp = 2.5;
lowTemp = 0;
TH2max = max(indexedImage(:))
thermalImage = lowTemp + (highTemp - lowTemp) * mat2gray(indexedImage);
subplot(2, 3, 3);
imshow(thermalImage, []);
colormap('hot');
colorbar;
title('2 Transverse Slits');
hp = impixelinfo();
hp.Units = 'normalized';
hp.Position = [0.45, 0.03, 0.25, 0.05];
ImgTH2mean = mean(thermalImage(:))

indexedImage = imgaussfilt(rgb2gray(TH4s),1);
highTemp = 2.5;
lowTemp = 0;
TH4max = max(indexedImage(:))
thermalImage = lowTemp + (highTemp - lowTemp) * mat2gray(indexedImage);
subplot(2, 3, 6);
imshow(thermalImage, []);
colormap('hot');
colorbar;
title('4 Transverse Slits');
hp = impixelinfo();
hp.Units = 'normalized';
hp.Position = [0.45, 0.03, 0.25, 0.05];
ImgTH4mean = mean(thermalImage(:))


%% subpolots ======================================================================
figure(2);
colormap(hot);
subplot(2,3,1)
imshow(T0, [])
title('AED T0 Image')
subplot(2,3,2)
imshow(TH2, [])
title('AED TH2 Image')
subplot(2,3,3)
imshow(TV2, [])
title('AED TV2 Image')
subplot(2,3,4)
imshow(T1, [])
title('AED T1 Image')
subplot(2,3,5)
imshow(TH4, [])
title('AED TH4 Image')
subplot(2,3,6)
imshow(TV4, []);
title('AED TV4 Image')

```